Journal of Statistical Physics, Vol. 66, Nos. 1/2, 1992

Phase Diagram of a Random Tiling Quasicrystal

Weixiong Li,[1,2] Hyunggyu Park,[1,3] and Michael Widom[1]

Received December 13, 1990; final August 2, 1991

We study the phase diagram of a two-dimensional random tiling model for quasicrystals. At proper concentrations the model has 8-fold rotational symmetry. Landau theory correctly gives most of the qualitative features of the phase diagram, which is in turn studied in detail numerically using a transfer matrix approach. We find that the system can enter the quasicrystal phase from many other crystalline and incommensurate phases through first-order or continuous transitions. Exact solutions are given in all phases except for the quasicrystal phase, and for the phase boundaries between them. We calculate numerically the phason elastic constants and entropy density, and confirm that the entropy density reaches its maximum at the point where phason strains are zero and the system possesses 8-fold rotational symmetry. In addition to the obvious application to quasicrystals, this study generalizes certain surface roughening models to two-dimensional surfaces in four dimensions.

KEY WORDS: Quasicrystals; random tiling models; phase diagram; domain walls; incommensurate phases; Landau theory; multicritical points; Hubbard model.

1. INTRODUCTION

The discovery of quasicrystals[1] revealed an entirely new class of solid structures beyond the classification of conventional crystallography. These structures were first found in rapidly solidified alloys such as AlMn, where electron diffraction patterns showed sharp peaks with icosahedral symmetry. Later on, materials with 8-fold,[2] 10-fold,[3] and 12-fold[4] symmetries were also found.

[1] Department of Physics, Carnegie Mellon University, Pittsburgh, Pennsylvania 15213.
[2] Current address: Department of Materials Science and Engineering, University of Pittsburgh, Pittsburgh, Pennsylvania 15261.
[3] Current address: Department of Physics, Boston University, Boston, Massachusetts 02215.

0022-4715/92/0100-0001$06.50/0

The local preference for icosahedral clusters at low temperatures in some materials has been known for many years.[5] In computer simulations of Lennard-Jones particles a small degree of extended orientational order was observed.[6] The possibility of such a phase with long-range orientational order but no translational order was later explored by Haymet[7] in the mean field approximation and a first-order transition from the liquid to such a phase was suggested. But the discovery of quasicrystals was certainly a big surprise, as the sharpness of the diffraction peaks requires long-range translational order.

Several models have been proposed to understand the mechanism responsible for the coexistence of long-range translational order and orientational order with noncrystallographic rotational symmetry. The icosahedral glass model[8,9] assumes that atoms prefer to form icosahedral clusters, which are then randomly packed together without overlapping with each other. Additional rules are imposed so as to generate the desired long-range icosahedral orientational order. These rules require icosahedral clusters to join each other vertex-to-vertex, edge-to-edge, or face-to-face, respectively. All three schemes provide similar results that are in good qualitative agreement with early experiments. However, since it is impossible to tile the entire space with icosahedra, long-range translational order is destroyed by defects. As a result, the translational order only propagates about several hundred angstroms, resulting in finite-width diffraction peaks.

Penrose tilings provided the first nontrivial example of a structure which is quasiperiodic with noncrystallographic rotational symmetry.[10–12] The perfect quasiperiodicity, which gives δ-function diffraction peaks, is maintained through restrictive matching rules. Based on such a ground state, fluctuations are introduced at finite temperatures in the form of matching rule violations.[13] One of the important questions concerning the Penrose model is whether the long-range translational order associated with the quasiperiodicity in the ground state can persist at finite temperatures. While Kalugin's arguments suggest a zero-temperature roughening transition out of the Penrose tiling state,[14] as was also argued and confirmed in the Monte Carlo simulation by Tang and Jaric,[15] this matter is still not completely settled.[13]

It was first pointed out by Elser[16] that matching rules in the Penrose model need not be solely responsible for the sharp diffraction patterns with noncrystallographic rotational symmetry. In his scheme, now called a "random tiling" model, quasicrystals can be viewed as random packings of two or more different kinds of cells without overlaps and gaps. The random tiling model possesses a large amount of entropy associated with matching rule violations. Such a random tiling model in equilibrium has quasi-long-

range translational order generating zero-width power-law peaks in two dimensions and δ-function Bragg peaks in three dimensions. Elser[16] and Henley[17] further conjectured that at the tile concentrations where the rotational symmetry is restored and the average phason strains are zero, the entropy density reaches its maximum. For small phason strains they postulated a quadratic dependence of entropy density on the phason strains.

Monte Carlo simulations of model binary atomic systems with Lennard-Jones interactions revealed structures close to those proposed by the random tiling model.[18–20] Many configurations exist that have energies close to each other, giving rise to a considerable amount of entropy. In fact, such near degeneracy becomes exact when the interaction potentials are truncated to the nearest neighbors. Further Monte Carlo simulations of the atomic system, its binary random tiling approximation, and a fully random tiling approximation were reported[21] and were compared with the results from transfer matrix calculation for binary tilings.[22] All these calculations show the existence of quasi-long-range translational order. It is intriguing that all these calculations give the same phason elastic constants within their numerical accuracies.

Most of the early quasicrystalline samples were prepared from the melt under rapid solidification, and thus were in metastable states. Furthermore, they all showed diffraction peaks with finite widths,[23] indicating large amounts of structural disorder which was widely believed then to be intrinsic to quasicrystals. These linewidths are narrower than those predicted by the icosahedral glass model, but wider than the predictions of the tiling models. More recently, equilibrium quasicrystals such as AlCuFe[24] and AlCuRu[25,26] were obtained using conventional solidification. Diffraction peaks with resolution-limited widths were reported, which seems to rule out the icosahedral glass model for these compounds. Moreover, careful measurements of peak intensities revealed that many intensities increase with temperature,[27] which is quite unusual, since in regular crystals phonon fluctuations, which increase with temperature, tend to reduce the peak intensities through the Debye–Waller factor. Widom[28] and Henley[29] pointed out that this observation supports random tiling models over the Penrose model because the phason elastic constants should increase with temperature in random tiling models.

An important problem in the study of quasicrystals remains the detailed examination of phase transitions to ordinary crystal structures at low temperatures.[30–32] The present paper studies the phase diagram of a two-dimensional random tiling model which is able to exhibit 8-fold rotational symmetry when uniform phason strains are absent. Geometrical properties of the 8-fold symmetric Penrose tiling have been studied by

several authors,[2,33] but the thermodynamic properties of the 8-fold random tiling model have not been explored. As will be shown in this paper, the quasicrystal phase (with phason strains in general) is well described by two sets of domain walls running in different directions. Thus, we consider the quasicrystal as a structure which is incommensurate in all spatial dimensions. The system can enter the quasicrystal phase from crystal phases through first-order transitions or continuous transitions. In addition, it can undergo two successive phase transitions corresponding to the introduction of two sets of domain walls, respectively. We numerically calculate the phason elastic constants and entropy density and confirm Elser and Henley's hypothesis that entropy density is maximum at points with zero phason strain.

The paper is organized as follows: Section 2 is devoted to general concepts about random tiling models. Most of the discussion applies with minor modifications to random tiling models with other rotational symmetries. Section 2.1 discusses the thermodynamic description of the model, while Section 2.2 applies the projection method to represent the tiling model as a surface roughening model in a space of four dimensions. Section 2.3 introduces the notion of De Bruijn lines and discusses their relations with domain walls in incommensurate phases. Section 2.4 introduces phason strains and relates tile densities with phason strains. Constraints among tile densities are derived and their consequences are discussed. Among the important consequences of these constraints is the locking of the quasicrystal state over a range of chemical potentials (discussed in greater detail in Section 4.1). Section 2.5 introduces a lattice model and also provides a transformation between the lattice model and the original tiling model. Section 2.6 relates the maximum tiling entropy density to the chemical potentials at the maximum.

Section 3 mainly outlines the various approaches we employ in this paper to study the model. Section 3.1 identifies all the possible phases and briefly discusses possible phase coexistence and phase transitions. Section 3.2 discusses an exact solution of our model in the incommensurate phase. The chief problem addressed in this paper is the extension of our understanding of the incommensurate phase to an understanding of the more general quasicrystal phase. We do this through a combination of a Landau theory of interacting incommensurate phases, and numerical transfer matrix calculations. The details of the numerical transfer matrix are discussed in Section 3.3, and Section 3.4 derives a Landau free energy density expansion in the limit of small domain wall densities.

Section 4 provides various cross sections of the phase diagram. Section 4.1 considers the phase diagram along the 8-fold symmetric line and discusses the phenomenon of locking on the quasicrystal compositions.

Sections 4.2 and 4.3 give 4-fold and 2-fold symmetric cross sections of the phase diagram, respectively. The phase diagrams presented in this section represent conjectures based on a combination of exact solutions and Landau theory backed up by numerical transfer matrix studies.

Section 5 studies multicritical points in the model. Section 5.1 provides cross sections of the phase diagram containing the multicritical points. Section 5.2 studies the multicritical points using the Landau free energy discussed in Section 3.4, while Section 5.3 provides numerical evidence that supports the results of Landau theory.

Section 6 contains several topics that are not covered in the previous sections, but are important and interesting. Section 6.1 defines the phason elastic constants and gives their numerical values. This calculation is tantamount to a confirmation of logarithmic surface height fluctuations, and power law diffraction peaks. Section 6.2 considers the possibility of coexistence of phason strained quasicrystal states. That is, in Section 4 we present two alternative phase diagrams. In Section 6.2 the question of which of the two is correct is examined, but not resolved. Section 6.3 studies the asymptotic degeneracy of the transfer matrix eigenvalues and Section 6.4 examines the finite-size corrections to the free energy inside the quasicrystal phase. Section 6.5 discusses the phase transition from the incommensurate phase to the quasicrystal phase. Section 6.6 discusses the interesting connection between our tiling model and the one-dimensional Hubbard model and also compares the phase diagrams of these two models. Section 6.7 gives a brief discussion of the possible generalization of this study to other quasicrystal systems in two and three dimensions, and Section 6.8 concludes the paper.

The chief contributions of this paper are the thermodynamic analysis of tiling models and the lattice model presented in Sections 2.1, 2.5, and 2.6; the description of quasicrystals in terms of fluctuating and interacting domain walls in Sections 2.3, 3.2, and 3.4; and finally the presentation of the phase diagram in Sections 4 and 5.1. Other important contributions of this work are the explanation of "locking" on the quasicrystal phase in Section 4.1, and numerical determination of quasicrystal entropy and elastic constants in Sections 4.2 and 6.1. Of technical note is the possibility that Landau expansions describe the exact behavior of continuous transitions into the quasicrystal phase as generalizations of commensurate–incommensurate phase transitions. For greater detail on our numerical calculations, our study of the Hubbard model, and also additional introductory material, we refer the reader to ref. 34.

2. QUASICRYSTALS WITH EIGHTFOLD SYMMETRY

2.1. The Model

Our model consists of two types of tiles, squares and 45° rhombi. The number grows to six if different orientations are taken into account. All the edge lengths are equal and set to be one. Each tile has a corresponding chemical potential associated with it, as is shown in Fig. 1. These chemical potentials serve to control the relative tile concentrations and generate phason strains. A naming scheme is shown in Fig. 2, in which each tile is labeled according to the vectors

$$\hat{e}_\alpha^{\parallel} \equiv \left(\cos \frac{\pi\alpha}{4}, \sin \frac{\pi\alpha}{4} \right) \qquad (\alpha = 0, 1, 2, 3) \tag{1}$$

which form its edges. Thus, a pair of integers $\alpha\beta$ $(\alpha \neq \beta)$ corresponds to a certain type of tile. There is a certain ambiguity in distinguishing between $(\alpha\beta)$ and $(\beta\alpha)$. As a convention, we shall in the rest of this paper label tiles with only those integer pairs $(\alpha\beta)$ which satisfy $\alpha < \beta$. That is,

$$(\alpha\beta) \in \{(01), (12), (23), (03), (02), (13)\} \tag{2}$$

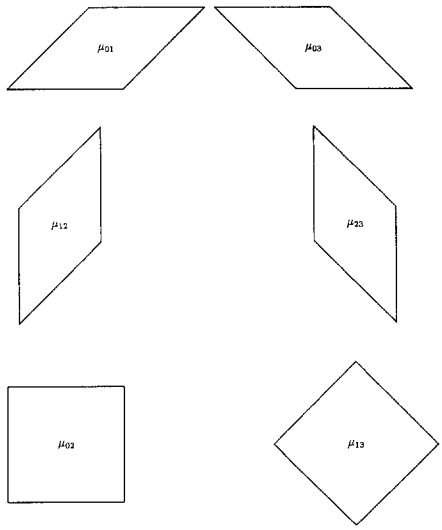

Fig. 1. The tiles and their chemical potentials. Tiles are labeled according to the two vectors which form them (Fig. 2a).

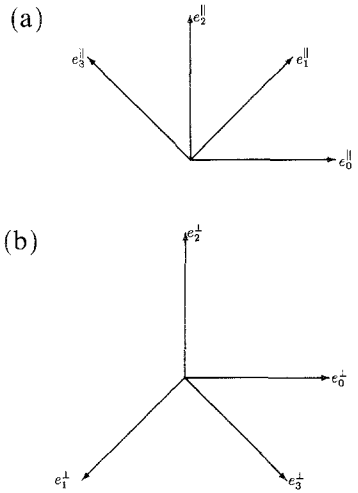

Fig. 2. Projection of 4-dimensinal hypercubic basis vectors into (a) parallel space and (b) perpendicular space. In the physical parallel space any vertex can be expressed as an integer sum of $\hat{e}_\alpha^{\parallel}$.

We concern ourselves primarily with the dependence of the entropy on compositions,

$$S = S(U, A, N_{01}, N_{12}, N_{23}, N_{03}, N_{02}, N_{13}) \tag{3}$$

where $N_{\alpha\beta}$ is the number of tiles with edges $\hat{e}_\alpha^{\parallel}$ and $\hat{e}_\beta^{\parallel}$,

$$A = N_{02} + N_{13} + \frac{1}{\sqrt{2}}(N_{01} + N_{12} + N_{23} + N_{03}) \tag{4}$$

is the area, and

$$U \equiv 0 \tag{5}$$

is the internal energy. Ordinarily, one expects the energy of an r-component system to depend on $r+2$ quantities; the r particle numbers or their chemical potentials, area or pressure, and energy or temperature. For our simple model, however, Eq. (4) shows that the area is uniquely determined by the tile numbers because we demand that tiles fill space without gaps or overlaps. Equation (5) shows that temperature plays no role because all configurations are assigned equal energy.

Thus we take the six tile numbers $N_{\alpha\beta}$ $(\alpha < \beta = 0, 1, 2, 3)$ or their conjugate chemical potentials $\mu_{\alpha\beta}$ as our independent parameters. Pressure drops out due to the Euler relation

$$S = \frac{1}{T} U + \frac{P}{T} A - \sum_{\alpha<\beta=0}^{3} \frac{\mu_{\alpha\beta}}{T} N_{\alpha\beta} \tag{6}$$

Since A is a linear combination of the $N_{\alpha\beta}$ by Eq. (4), we may absorb pressure into the chemical potentials

$$\mu_{\alpha\beta} \to \mu_{\alpha\beta} - Pa_{\alpha\beta} \tag{7}$$

where $a_{\alpha\beta}$ is the area of tile type $\alpha\beta$ ($a_{02} = a_{13} = 1$ for squares and $a_{01} = a_{12} = a_{23} = a_{03} = 1/\sqrt{2}$ for rhombi). Furthermore, temperature drops out because $U = 0$. We simply set $P = 0$ and $T = 1$ for the remainder of the paper. In terms of our new chemical potentials we have

$$S = -\sum_{\alpha < \beta = 0}^{3} \mu_{\alpha\beta} N_{\alpha\beta} \tag{8}$$

which we recognize as simply the negative of the Gibbs potential $G(T, P, \{N_{\alpha\beta}\})$. Of course, there also exists a Gibbs–Duhem relation among the six chemical potentials,

$$\sum_{\alpha < \beta = 0}^{3} N_{\alpha\beta}\, d\mu_{\alpha\beta} = 0 \tag{9}$$

so that our phase diagram is truly just five-dimensional.

Finally, we discuss how to relate the tile numbers to their conjugate chemical potentials. This is accomplished by a Legendre transformation replacing the entropy $S(\{N_{\alpha\beta}\})$ with a free energy density

$$F(\{\mu_{\alpha\beta}\}) = -S - \sum_{\alpha' < \beta' = 0}^{3} \mu_{\alpha'\beta'} N_{\alpha'\beta'}(\{\mu_{\alpha\beta}\}) \tag{10}$$

where the values of $\{N_{\alpha\beta}\}$ are chosen so that F is minimized. Clearly the minimum value is $F = 0$, in view of Eq. (8). This suggests that a solution of the model inside a particular phase is fully contained in a surface in the hyperspace spanned by the chemical potentials $\mu_{\alpha\beta}$,

$$F(\mu_{01}, \mu_{12}, \mu_{23}, \mu_{03}, \mu_{02}, \mu_{13}) = 0 \tag{11}$$

which simply puts a constraint among various chemical potentials and is just another manifestation of the Gibbs–Duhem relation, Eq. (9). The function F in general has distinct functional forms in different phases. First-order transitions between two phases A and B are located by combining the two equations

$$\begin{aligned} F_A(\mu_{01}, \mu_{12}, \mu_{23}, \mu_{03}, \mu_{02}, \mu_{13}) &= 0 \\ F_B(\mu_{01}, \mu_{12}, \mu_{23}, \mu_{03}, \mu_{02}, \mu_{13}) &= 0 \end{aligned} \tag{12}$$

because chemical potentials are continuous across the phase boundaries. Furthermore, since F contains no extensive variables, one cannot actually determine the values of $\{N_{\alpha\beta}\}$. Only the densities

$$d_{\alpha\beta} = \frac{N_{\alpha\beta}}{A} \tag{13}$$

are detemined.

2.2. The Projection Method

Tilings such as the one shown in Fig. 3a are conveniently described by the projection method.[35] Consider the four unit vectors $\hat{e}_\alpha^{\parallel}$ shown in Fig. 2a. Any tile vertex $\mathbf{R}^{\parallel} \in \Re^2$ in Fig. 3a can be expressed in terms of integer linear combination of $\hat{e}_\alpha^{\parallel}$ if the origin is chosen at an arbitrary vertex,

$$\mathbf{R}^{\parallel} = \sum_{\alpha=0}^{3} R_\alpha \hat{e}_\alpha^{\parallel} \tag{14}$$

where R_α are integers. This representation forms a mapping (or projection) between the vertices in the tiling and a subset of lattice points in a 4-dimensional hypercubic lattice. Let us denote the unit vectors of this 4-dimensional space by $\hat{a}_\alpha$, $\alpha = 0, 1, 2, 3$. The projected "parallel" space is spanned by

$$\hat{e}_x^{\parallel} = \frac{1}{\sqrt{2}} \hat{a}_0 + \frac{\hat{a}_1 - \hat{a}_3}{2} \tag{15}$$

$$\hat{e}_y^{\parallel} = \frac{1}{\sqrt{2}} \hat{a}_2 + \frac{\hat{a}_1 + \hat{a}_3}{2} \tag{16}$$

Since this projection maps a 4-dimensional space into the 2-dimensional physical space (or parallel space), there is another 2-dimensional space perpendicular to the parallel space, which we call "perpendicular" space. The unit vectors spanning the perpendicular space are defined as

$$\hat{e}_x^{\perp} = \frac{1}{\sqrt{2}} \hat{a}_0 - \frac{\hat{a}_1 - \hat{a}_3}{2} \tag{17}$$

$$\hat{e}_y^{\perp} = \frac{1}{\sqrt{2}} \hat{a}_2 - \frac{\hat{a}_1 + \hat{a}_3}{2} \tag{18}$$

We can define

$$\hat{e}_\alpha^{\perp} = (-1)^\alpha \left[\cos\left(\frac{\pi\alpha}{4}\right) \hat{e}_x^{\perp} + \sin\left(\frac{\pi\alpha}{4}\right) \hat{e}_y^{\perp} \right] \tag{19}$$

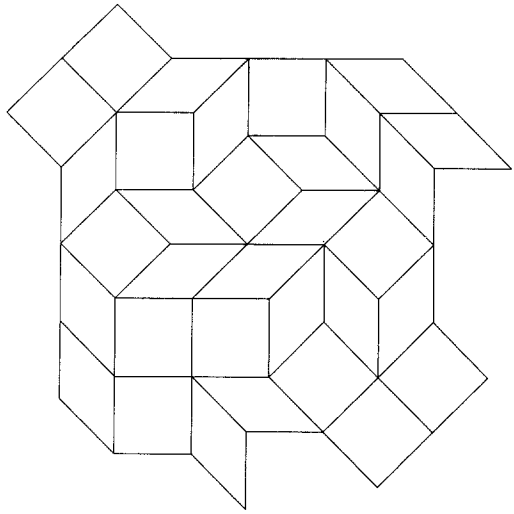

(a)

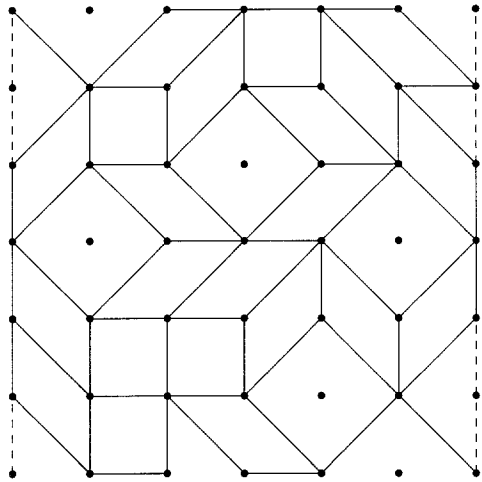

(b)

Fig. 3. (a) A typical tiling configuration. All configurations are allowed as long as tiles do not overlap with each other and there are no gaps in between tiles. (b) The same tiling configuration as in (a) after lattice distortion. Dots represent the lattice sites of the two-dimensional square lattice. Those isolated lattice sites correspond to the centers of tilted squares. Notice that after distortion each tilted square has area 2 and each rhombus has area 1. The broken lines represent the boundary, which simply cuts off those parts of tiles that are outside of the system.

which are shown in Fig. 2b, in analogy to the vectors $\hat{e}_\alpha^{\parallel}$ defined in Eq. (1) shown in Fig. 2a. It is easy to verify that $\sqrt{2}\,\hat{a}_\alpha = (\hat{e}_\alpha^{\parallel} + \hat{e}_\alpha^{\perp})$, and that a point $\mathbf{R} = \sqrt{2}\sum_{\alpha=0}^{3} R_\alpha \hat{a}_\alpha \in \Re^4$ falls on the point $\mathbf{R}^{\parallel}$ in Eq. (14) upon projection into the parallel plane. One thus finds that the lattice constant of this 4-dimensional hypercubic lattice is $\sqrt{2}$. There is a one-to-one correspondence between points $\mathbf{R}^{\parallel}$ of a tiling and points $\mathbf{R}/\sqrt{2} \in \mathbb{Z}^4$ of the hypercubic lattice. But we can also project into the perpendicular space

$$\mathbf{R}^{\perp} = \sum_{\alpha=0}^{3} R_\alpha \hat{e}_\alpha^{\perp} \tag{20}$$

so that Eqs. (14) and (20) together form a one-to-one mapping between parallel and perpendicular spaces.

Note that nearby vertices in the tiling correspond to nearby lattice points in the hypercubic lattice. Since all the tiling configurations are discrete on the scale of tile edges, it is useful to coarse grain over a length scale which is much greater than tile edges, but still negligibly small compared with system sizes. After coarse graining, the height in the perpendicular space becomes a smoothly varying function of position in parallel space $\mathbf{R}^{\perp}(\mathbf{R}^{\parallel})$. Thus, over large scales, one can view the random tilings as a fluctuating, but continuous 2-dimensional interface in the 4D hypercubic lattice. The requirement that tiles never overlap imposes a "solid-on-solid" constraint excluding overhangs in the fluctuating surface when viewed from the parallel space. The requirement that the plane be tiled without cracks excludes tears in this fluctuating surface. Two-dimensional surfaces fluctuating in 3D space model roughening of crystal facets. Our model is then a simple generalization of an ordinary roughening model where we can roughen into two extra dimensions instead of one. Perfectly flat surfaces, with $\mathbf{R}^{\perp}$ constant, correspond to deterministic quasiperiodic structures such as the one illustrated in Fig. 4.

2.3. De Bruijn Lines

Tiling models are equally well described by the dual method introduced by de Bruijn.[10] De Bruijn lines are those lines which connect centers of parallel edges. Drawn in Fig. 5a is a de Bruijn line which connects horizontal edges. Thus four types of de Bruijn lines exist in our model corresponding to four edge orientations. We name those lines which connect centers of $\hat{e}_\alpha^{\parallel}$ to be the αth type of de Bruijn line, and denote the density by n_α. De Bruijn lines of the same type never touch each other, while different types of de Bruijn lines may cross each other. Thus, de Bruijn lines in our model resemble domain walls, and we shall frequently refer to de Bruijn lines as domain walls.

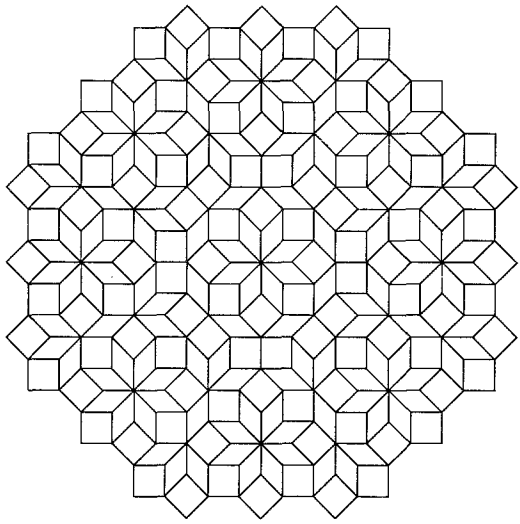

Fig. 4. A portion of the 2-dimensional 8-fold symmetric Penrose tiling. It is perfectly quasiperiodic and possesses Bragg diffraction peaks. (Taken from ref. 2.)

De Bruijn lines have well-defined average positions and orientations in a uniform phase. Fluctuations away from such average lines grow at most as the square root, and usually only as the logarithm of system size. For perfect Penrose patterns, the de Bruijn lines have only bounded fluctuations. Furthermore, their orientations are perpendicular to the edges they connect, so that they intersect with one another at well-defined angles (multiples of 45°). However, in general the orientation of the αth type of domain wall is not perpendicular to $\hat{e}_\alpha^{\parallel}$ and one has to define the domain wall density very carefully. A convenient definition is to measure the number of the αth type of domain wall in the direction of $\hat{e}_\alpha^{\parallel}$,

$$n_\alpha = \frac{N_\alpha}{L} \tag{21}$$

where L is the length of a line parallel to $\hat{e}_\alpha^{\parallel}$ and N_α is the number of the αth type of domain wall crossing the line.

2.4. Phason Strains

The Penrose tiling and its generalizations to other strictly quasiperiodic structures (Fig. 4) correspond to deterministic surfaces in the hypercubic lattice which are flat instead of rough at all but microscopic

scales. However, quasicrystals, defined to be materials possessing sharp diffraction peaks with noncrystallographic rotational symmetry, belong to a more general class of tiling configurations whose hypersurfaces need be flat only over large scales. The quasiperiodic Penrose tiling is only one of many members of this set. This wider class of tilings correspond to hypersurfaces which possess an approximating plane, which is defined such that the distance between the hypersurfaces and the approximating plane $d(\mathbf{R}^{\parallel})$ grows more slowly than $\mathbf{R}^{\parallel}$:

$$\lim_{\mathbf{R}^{\parallel}\to\infty} \frac{d(\mathbf{R}^{\parallel})}{|\mathbf{R}^{\parallel}|} \to 0 \tag{22}$$

This approximating plane can be parameterized as

$$R_\alpha = \mathbf{m}_\alpha \cdot \mathbf{R}^{\parallel} + \text{constant}, \qquad \alpha = 0, 1, 2, 3 \tag{23}$$

where $\{\mathbf{m}_\alpha\}$ is a set of four two-dimensional vectors which define the orientation of the plane, and R_α and $\mathbf{R}^{\parallel}$ are now continuous variables describing the coarse-grained surface as discussed in Section 2.2. Any arbitrary point in the 4-dimensional hyperspace can be expressed as $\mathbf{R} = \sum_{\alpha=0}^{3} R_\alpha(\hat{e}_\alpha^{\parallel} + \hat{e}_\alpha^{\perp})$, because $\mathbf{R} = \mathbf{R}^{\parallel} + \mathbf{R}^{\perp}$ by definition. Thus we get

$$R_\alpha = \tfrac{1}{2}(\hat{e}_\alpha^{\parallel} \cdot \mathbf{R}^{\parallel} + \hat{e}_\alpha^{\perp} \cdot \mathbf{R}^{\perp}) \tag{24}$$

We now combine Eqs. (23) and (24) to relate the orientation defined by $\{\mathbf{m}_\alpha\}$ to a quantity known as phason strain. Different classes of tiling configurations (which give different diffraction patterns in experiments) can be distinguished by their phason strains, which measure the long-range deviation in perpendicular space from the plane approximating the Penrose tiling. We ignore complications due to the notion of local isomorphism class, which appears to have no bearing on our random tiling models. The first derivatives of the function $\mathbf{R}^{\perp}(\mathbf{R}^{\parallel})$ form a matrix called the phason strain matrix

$$E_{ij} = \frac{\partial R_i^{\perp}}{\partial R_j^{\parallel}} \tag{25}$$

where i and j denote the x and y components. We will be concerned primarily with the uniform, or average, phason strain matrix, whose elements are just the four slopes of the two-dimensional approximating plane in four-dimensional space. Of course, there will be in general local fluctuations in E_{ij}. These fluctuations are precisely the source of entropy which motivates random tiling models. But these local fluctuations enter a thermodynamic description of the model *only* through the entropy. In

addition to local fluctuations of E_{ij}, one might have a configuration with different average strains in different regions of space. Such a configuration may be described as phase separation. There are two or more homogeneous thermodynamic states coexisting. In such cases an approximating plane cannot exist.

The projection method enables us to relate tile densities and phason strains. Tiles in the parallel space are projected square faces of unit cells in the 4-dimensional space. In fact, the tile densities $d_{\alpha\beta}$ are simply equal to the magnitude of the direction cosine relating the square face formed by $\hat{a}_\alpha$ and $\hat{a}_\beta$ (Section 2.2) to the approximating plane.[17] Denote by $d_{\alpha\beta}$ the area density of tiles whose edges are α- and β-type bonds. Then we have

$$d_{\alpha\beta} = \mathbf{m}_\alpha \times \mathbf{m}_\beta \tag{26}$$

The 2D cross product is simply the area of the parallelogram formed by $\mathbf{m}_\alpha$ and $\mathbf{m}_\beta$. In Eq. (26), $\mathbf{m}_\alpha$ is the orientation of the approximating plane given by

$$\begin{aligned} \mathbf{m}_\alpha &= \nabla_{||} R_\alpha \\ &= \tfrac{1}{2}(\hat{e}_\alpha^{||} + \hat{e}_\alpha^{\perp} \cdot \mathsf{E}), \qquad \alpha = 0, 1, 2, 3 \end{aligned} \tag{27}$$

Note that the signs of $d_{\alpha\beta}$ in Eq. (26) are positive for small phason strains if we follow the convention of Eq. (2). In the case where phason strains vanish, Eq. (27) gives $d_{01} = d_{12} = d_{23} = d_{03} = 1/(4\sqrt{2})$ and $d_{02} = d_{13} = 1/4$. In general

$$\begin{aligned} d_{01} &= \frac{1}{4\sqrt{2}}(1 + E_{xx} - E_{yy} - 2E_{xy} - \det \mathsf{E}) \\ d_{12} &= \frac{1}{4\sqrt{2}}(1 - E_{xx} + E_{yy} - 2E_{yx} - \det \mathsf{E}) \\ d_{23} &= \frac{1}{4\sqrt{2}}(1 - E_{xx} + E_{yy} + 2E_{yx} - \det \mathsf{E}) \\ d_{03} &= \frac{1}{4\sqrt{2}}(1 + E_{xx} - E_{yy} + 2E_{\dot{x}y} - \det \mathsf{E}) \\ d_{02} &= \frac{1}{4}(1 + \mathrm{Tr}\ \mathsf{E} + \det \mathsf{E}) \\ d_{13} &= \frac{1}{4}(1 - \mathrm{Tr}\ \mathsf{E} + \det \mathsf{E}) \end{aligned} \tag{28}$$

Thus, the four phason strain components completely determine the thermodynamic state of the tiling.

It should be pointed out that the six tile densities are not totally independent. Two constraints can be derived from Eq. (28),

$$d_{02} + d_{13} + \frac{1}{\sqrt{2}}(d_{01} + d_{12} + d_{23} + d_{03}) = 1 \tag{29}$$

and

$$2(d_{02} + d_{13}) = 1 + (d_{02} - d_{13})^2 - \tfrac{1}{2}(d_{01} + d_{03} - d_{12} - d_{23})^2 - 2(d_{23} - d_{12})(d_{03} - d_{01}) \tag{30}$$

Equation (29) simply reflects the condition of Eq. (4) that the tiles fill the plane. The physical origin for the nonlinear constraint (30) can be understood in terms of de Bruijn lines. Imagine describing a tiling by giving the total area and the number of all four types of rhombi. Then the bulk densities n_α of de Bruijn lines are fixed. But the densities d_{02} and d_{13} of squares are given by $n_0 n_2$ and $n_1 n_3$, respectively, since squares sit at the intersections of de Bruijn lines whose indices differ by 2. That is the origin of the nonlinear constraint (30). Of course, in some special phases where horizontal and vertical de Bruijn lines do not cross, one would expect Eq. (30) to be unnecessary. Indeed in these cases Eq. (30) becomes equivalent to Eq. (29).

The existence of constraint (30) indicates that the quasicrystal phase, in which all four types of de Bruijn lines are present, is described by only four parameters, so in our five-dimensional phase diagram there exist trajectories along which tile densities do not vary. An immediate application of this equation of constraint is the explanation of locking on the quasicrystal composition over a range of chemical potentials (see Section 4.1). However, since the nonlinear constraint (30) becomes identical to the area constraint (29) inside the four incommensurate phases, we lose one independent constraint. Therefore the fifth dimension of the phase diagram becomes important in describing the phase transitions out of the quasicrystal phase (with phason strains in general). This is consistent with our previous discussion in Section 2.1 [see the Gibbs–Duhem relation, Eq. (9)] that the whole phase diagram is five-dimensional. However, this fifth dimension is visible only in those phase regions where a unique approximating plane [defined in Eq. (22)] does not exist and Eq. (30) is violated, or in phases for which Eqs. (29) and (30) are redundant.

Finally, we point out that tile densities must not take negative values; thus,

$$d_{\alpha\beta} \geqslant 0 \tag{31}$$

Equation (31) puts further limits on phason strain components E_{ij}.

2.5. The Lattice Model

Because of the incommensurate nature of the tiling model, vertices in the tiling such as in Fig. 3a form an irregular network. This makes study of the model technically difficult. Distorting the tiles so that vertices of the tiling all sit at lattice points on the square lattice resolves this problem. This is done explicitly by stretching the lengths of all diagonal bonds by a factor of $\sqrt{2}$ while leaving the horizontal and vertical bonds unchanged. Figure 3b shows the tiling in Fig. 3a after such distortion. Note that square lattice points which are not occupied by the tiling vertices correspond to centers of tilted squares [tiles of type (13)].

The lattice distortion as introduced above obviously preserves all the topological properties of the original tiling. However, such a distortion does change the meaning of the chemical potentials which are supposed to control the relative concentrations of tiles, because the areas of tilted squares and rhombi get increased by factors of 2 and $\sqrt{2}$, respectively, after the lattice distortion. As a result, for example, in a given area we can now accommodate more squares than we can accommodate tilted squares. This means the lattice distortion discriminates against tilted squares and rhombi. Correction of such bias[17,22,36,37] is important if our final phase diagram is to be presented in a way which preserves the symmetry between the two types of squares and the physical meaning of chemical potentials.

Thus, two sets of chemical potentials should be distinguished. One set is defined by thermodynamic relations and we call them canonical chemical potentials

$$\mu_{\alpha\beta} = -\frac{\partial S}{\partial N_{\alpha\beta}} \tag{32}$$

where $\alpha < \beta = 0, 1, 2, 3$ and S is the total entropy of the system. Because the total entropy is unaffected by the lattice distortion, they are the true chemical potentials of the undistorted tiles, and thus should exhibit all the symmetries that the tiles have. For an example, a 45° rotation interchanges squares and tilted squares; thus, we will expect to see the transformation $\mu_{02} \leftrightarrow \mu_{13}$ under this rotation. Notice that these canonical chemical potentials are in general nonpositive, since adding tiles cannot decrease the entropy.

Another set of chemical potentials, which we denote by $\bar{\mu}_{\alpha\beta}$, where $(\alpha\beta)$ again goes over all types of tiles, are the parameters that we assign to the tiles after lattice distortion so as to control the tile concentrations in our lattice model. These chemical potentials will not reflect the proper symmetries that the undistorted tiles have among themselves. The transformation between $\mu_{\alpha\beta}$ and $\bar{\mu}_{\alpha\beta}$ will now be derived.

Consider a general tiling problem in which there are r types of tiles. Let $\bar{a}_k$ be the area of kth type of tile after lattice distortion. The total area of the distorted tiling is

$$\bar{A} = \sum_{k=1}^{r} N_k \bar{a}_k \tag{33}$$

The total entropy is a homogeneous function of tile numbers satisfying

$$S(\{N_k\}) = -\sum_{k=1}^{r} \mu_k N_k \tag{34}$$

The entropy density per *lattice area*

$$\bar{\sigma}(\{y_k\}) = \frac{S(\{N_k\})}{\bar{A}} \tag{35}$$

is related to the chemical potentials through

$$\bar{\sigma}(\{y_k\}) = -\sum_{k=1}^{r} \nu_k y_k \tag{36}$$

where the fractional on-lattice area occupied by the kth type of tile is

$$y_k = \frac{N_k \bar{a}_k}{\bar{A}} \tag{37}$$

and the chemical potential per tile area is

$$\nu_k = \frac{\mu_k}{\bar{a}_k} \tag{38}$$

Note that $\{y_k\}$ satisfies the constraint $\sum_k y_k = 1$ and thus the fractional areas are not totally independent parameters. Without loss of generality we may write $y_r = 1 - \sum_{j=1}^{r-1} y_j$. Taking the partial derivative of Eq. (36) with respect to y_k while holding all the other fractional areas fixed yields

$$\frac{\partial \bar{\sigma}}{\partial y_k} = \nu_r - \nu_k \tag{39}$$

after application of the Gibbs–Duhem relation, Eq. (9).

Now consider the canonical partition function defined on the lattice

$$Z = \sum_{\text{conf}} \exp\left(\sum_{k=1}^{r} N_k \bar{\mu}_k \right) \tag{40}$$

where the sum includes all configurations occupying the area $\bar{A}$. In the thermodynamic limit one expects

$$\log Z = \max_{\{N_k\}} \left[S(N_k) + \sum_{k=1}^{r} N_k \bar{\mu}_k \right] \tag{41}$$

subject to the constraint $\sum N_k \bar{a}_k = \bar{A}$, and thus

$$\psi \equiv \frac{1}{\bar{A}} \log Z = \max \left[\bar{\sigma} + \sum_{k=1}^{r} y_k \bar{\nu}_k \right] \tag{42}$$

subject to the constraint $\sum y_k = 1$, where $\bar{\nu}_k = \bar{\mu}_k / \bar{a}_k$. Expression (42) requires

$$\frac{\partial \bar{\sigma}}{\partial y_k} = \bar{\nu}_r - \bar{\nu}_k \tag{43}$$

which, when combined with Eq. (39), gives

$$\bar{\nu}_k = \nu_k + c \tag{44}$$

where c is independent of k. Multiplying Eq. (44) by y_k, then comparing with Eqs. (42) and (36), we see that $c = \psi$. Thus we have derived a set of transformations between the two sets of chemical potentials:

$$\mu_k = \bar{\mu}_k - \bar{a}_k \psi, \qquad k = 1, 2, \ldots, r \tag{45}$$

For our distorted tiling model we have $\bar{a}_{01} = \bar{a}_{12} = \bar{a}_{23} = \bar{a}_{03} = \bar{a}_{02} = 1$ and $\bar{a}_{13} = 2$. Thus, Eq. (45) becomes

$$\begin{aligned} &\mu_{\alpha\beta} = \bar{\mu}_{\alpha\beta} - \psi, \qquad (\alpha\beta) = (01), (12), (23), (03), (02) \\ &\mu_{13} = \bar{\mu}_{13} - 2\psi \end{aligned} \tag{46}$$

One immediately sees that a shift of $\bar{\mu}_{\alpha\beta}$ by

$$\begin{aligned} &\bar{\mu}_{\alpha\beta} \to \bar{\mu}_{\alpha\beta} + \delta, \qquad (\alpha\beta) = (01), (12), (23), (03), (02) \\ &\bar{\mu}_{13} \to \bar{\mu}_{13} + 2\delta \end{aligned} \tag{47}$$

leaves the canonical chemical potentials invariant. This explicitly shows that the whole phase diagram is 5-dimensional, which is consistent with our previous discussion in Sections 2.1 and 2.4. Throughout our entire calculation on the lattice model we will choose δ to set $\bar{\mu}_{13} = 0$.

2.6. Point of Maximum Entropy Density

Finally, in this subsection, we relate the chemical potentials at the maximum entropy density point to the value of maximum entropy density. Let a_k be the area of the kth type of tile (undistorted) and $x_k = N_k a_k / A$ be the fractional area of the kth type of tile, where $A = \sum_k N_k a_k$ is the total tiling area. The off-lattice entropy density

$$\sigma \equiv \frac{S(\{N_k\})}{A} = -\sum_{k=1}^{r} \frac{\mu_k}{a_k} x_k \tag{48}$$

Taking the derivative of σ with respect to x_k, we find

$$\frac{\partial \sigma}{\partial x_k} = \frac{\mu_r}{a_r} - \frac{\mu_k}{a_k} \tag{49}$$

in analogy with Eq. (39). At the entropy maximum point the partial derivatives in Eq. (49) vanish and we find

$$\mu_k = -a_k \sigma_0, \qquad k = 1, 2, \ldots, r \tag{50}$$

where σ_0 is the maximum entropy density.

For our model we then have

$$\mu_{01} = \mu_{12} = \mu_{23} = \mu_{03} = -\frac{\sigma_0}{\sqrt{2}} \qquad \text{and} \qquad \mu_{02} = \mu_{13} = -\sigma_0 \tag{51}$$

Equation (50) is a generalization of results obtained by Widom *et al.*[22] and Shaw and Henley[36] in their studies of 10-fold tilings. Equation (51) will be numerically verified. Since in practice all these quantities such as the μ's and σ_0 are obtained through extrapolation, Eq. (51) provides a severe test to the extrapolation techniques we use. We note here, however, that in the thermodynamic limit $\sigma(\{x_k\})$ is not differentiable with respect to the x_k at the quasicrystal density. Thus, we actually find a line segment in the space of variables $\{\mu_k\}$ corresponding to the quasicrystal state. The point of entropy maximum extrapolated from finite-size data is a unique point on this line segment obeying Eq. (51). We discuss this further in Section 4.1.

3. PHASE IDENTIFICATION AND NUMERICAL TECHNIQUES

This section discusses various techniques we shall use to study the model. We first identify the quasicrystal phase, the incommensurate phases, and the crystal phases, and discuss the notion of phase coexistence and

possibility of phase transitions. Then an exact solution is given inside the incommensurate phases by mapping onto the six-vertex model. Inside the general quasicrystal phase no exact solution is yet obtained, and we describe the application of the transfer matrix approach to the model. Finally, in the limit of small domain wall densities we propose a Landau theory of the quasicrystal entropy.

3.1. Phases, Phase Coexistence, and Phase Transitions

We have identified 11 distinct phases:

(1, 2) C_{02}, C_{13}: crystal phases with only (02) and (13) squares, respectively.

(3–6) C_{01}, C_{12}, C_{23}, C_{03}: crystal phases with only one type of rhombus.

(7) I_0: an incommensurate phase with (01), (03) rhombi and (13) squares.

(8) I_1: an incommensurate phase with (01), (12) rhombi and (02) squares.

(9) I_2: an incommensurate phase with (12), (23) rhombi and (13) squares.

(10) I_3: an incommensurate phase with (23), (03) rhombi and (02) squares.

(11) Q: phason strained quasicrystal phase.

In addition, there is the phason-strain-free quasicrystal structure, which we shall denote ϕ, although it is not thermodynamically distinct from Q. The crystal phases $C_{\alpha\beta}$ have two types of domain walls missing, and the incommensurate phases I_α have only one type of domain wall missing. The quasicrystal phase Q contains all four types of domain walls.

Figure 5a shows a typical configuration of the I_0 phase. The C_{02} and C_{13} phases are simply square lattices. The Q phase is illustrated in Fig. 3a. Note that under 45° rotations these phases transform,

$$\begin{aligned} &C_{02} \to C_{13} \to C_{02} \\ &C_{01} \to C_{12} \to C_{23} \to C_{03} \to C_{01} \\ &I_0 \to I_1 \to I_2 \to I_3 \to I_0 \\ &Q \to Q \end{aligned} \tag{52}$$

Of course, such symmetries among these phases are broken in the lattice model because the areas of squares (02) and tilted squares (13) are

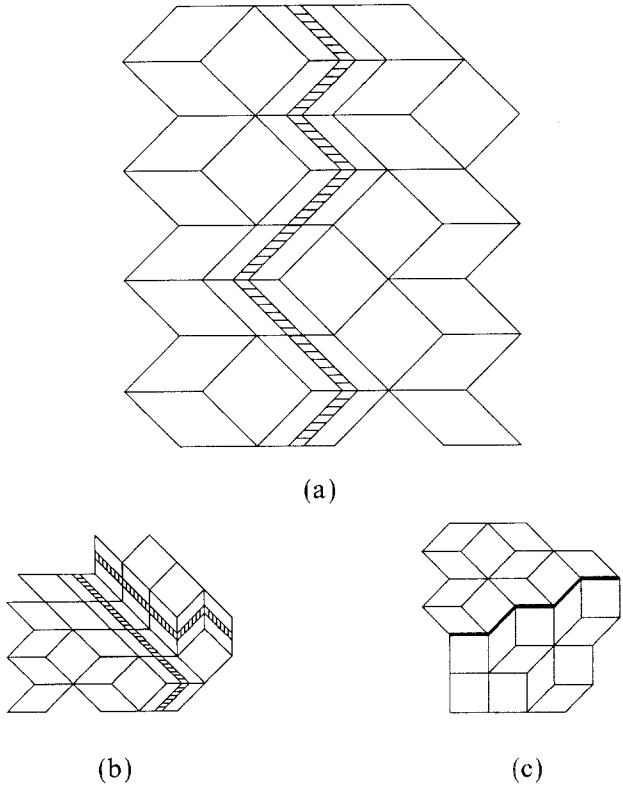

Fig. 5. (a) A typical configuration of the I_0 phase. Successive 45° rotations transform the I_0 phase into I_1, I_2, and I_3 phases. Type 0 domain walls connect centers of horizontal edges of rhombi. (b) Coexistence of I_0 and I_2. Domain walls such as those shaded become rigid. (c) Coexistence of I_0 and I_1. The thick line represents the phase boundary.

unequal. Symmetries among the tile numbers $N_{\alpha\beta}$ need not imply symmetries among on-lattice chemical potentials $\bar{\mu}_{\alpha\beta}$. Still, 90° rotations which interchange I_0 with I_2 and I_1 with I_3 while leaving C_{02} and C_{13} invariant are symmetric operations on lattice as well as off lattice.

The question of phase coexistence is quite subtle due to the strict geometrical constraints. We discuss the various cases in the following.

1. C_{02} and C_{13}. These two square phases are not compatible with each other. Tears must be introduced between the two phases. Since such tears possess infinite energies in the random tiling models, interfaces between these phases have infinite energies. The phases can touch at most at a single vertex.

2. I_0 and I_2. Geometrically, these two phases can coexist, as is shown in Fig. 5b. However, such a coexistence reduces the entropy by an amount quadratic in the interface length because the type 0 and type 2 walls cannot cross. Thus, interfaces in this case have infinite free energies. A similar situation occurs for I_1 and I_3. These phases will touch only on interfaces of finite length.

3. I_0 and I_1. These two phases coexist with relative ease, as is demonstrated in Fig. 5c. Because of this, all four incommensurate phases I_α can also coexist without introducing interfaces with infinite free energies. But the spatial arrangement of the coexisting phases is not completely free. For instance, it is impossible to *completely* surround one phase with another. Even when the interfacial free energy is infinite, we shall still speak of "coexisting phases" whenever these phases are equal in free energy.

We also note that the four incommensurate phases are well described by a single family of noncrossing domain walls running in one of the four directions. For example, the phase I_0 pictured in Fig. 5a can be described as a tilted square lattice with domain walls connecting horizontal edges of the (01) or (03) rhombi. It is interesting to note that this domain wall family is just one of the sets of dual lines, or "de Bruijn lines," of the tiling. The other two sets of dual lines make up a lattice in which the domain wall meanders. It is this analogy with domain wall models that makes exact solutions possible in these phases.

Phase transitions among the phases can all be described in terms of domain walls. In the following discussions we will not try to argue that such transitions must happen. Rather, based on the assumption that they do occur, we try to understand their nature. The validity of these assumptions is the subject of the remainder of the paper.

1. Crystal phases $C_{\alpha\beta}$ to incommensurate phase I_γ. These are conventional commensurate–incommensurate phase transitions. We discuss these in the phenomenological theory of Pokrovsky–Talapov and also present exact solutions.

2. Crystal phase $C_{\alpha\beta}$ to quasicrystal phase Q. This transition corresponds to introducing two sets of domain walls simultaneously. We shall see in the following sections that such a transition is in general first order. However, a continuous phase transition is possible if chemical potentials of the tiles satisfy certain relations, resulting in a multicritical point.

3. Incommensurate phase I_α to quasicrystal phase Q. This phase transition requires tiles containing the edges that are missing in I_α. However, as shown in Fig. 6, an entire string of such bonds have to be

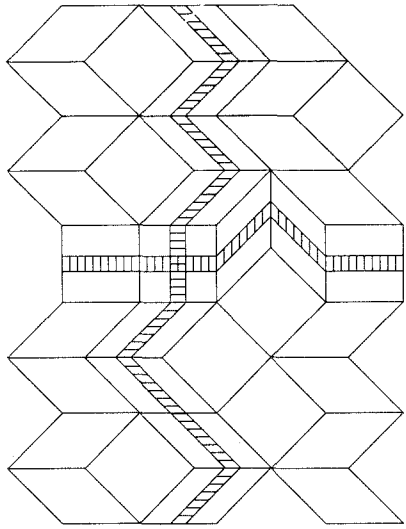

Fig. 6. A complete string of vertical bonds must be introduced in order to enter the quasicrystal phase from the I_0 phase. This string is easily recognized as a type 2 domain wall. Note that the squares are located at the intersection of type 0 and type 2 domain walls.

introduced in order to avoid gaps and overlaps between tiles. Such a phase transition is quite novel, since it introduces domain walls in an incommensurate background, in which another set of domain walls go in the perpendicular direction. As we shall see later, Landau theory suggests that such a transition can be either first order or continuous.

4. There are regions in the phase diagram in which the two of the incommensurate phases with the same type of squares may coexist, for example, I_0 and I_2 may coexist when the chemical potentials of the rhombi are the same. Phase coexistence alters the nature of phase transitions into the quasicrystal phase. As we have pointed out, the transition from any of I_α into Q can be continuous. However, we can argue that the transition from $I_\alpha \oplus I_\beta$ to Q, where I_α and I_β share the same type of squares [i.e., $\alpha = (\beta + 2) \bmod 2$], will in general be first order. Mixing of I_α and I_β requires the other type of missing squares at the intersections of the domain walls. The density of these new squares $d_{\alpha\beta}$ is the product of the domain wall densities n_α and n_β in the I_α and I_β phases, which means the density of the missing squares has a discontinuous jump and the phase transition is first order.

From the above discussions we conclude that the quasicrystal phase is actually surrounded in the phase diagram by these other phases. The

system can enter the quasicrystal phase either from the crystal phases directly or go through intermediate incommensurate phases.

3.2. Exact Solutions in the Incommensurate Phases

As we have discussed in the previous subsection, there are in total four incommensurate phases, each of which contains one relevant type of domain wall. Exact solutions are obtained by mapping the systems onto exactly solvable six-vertex models[38] with some particular correspondence between tile configurations and vertex configurations (Fig. 7). Detailed studies have been reported earlier elsewhere[39]; here we mainly concentrate on the transition line and the entropy density associated with the random tiling.

Each of the four incommensurate phases consists of two kinds of rhombus and one kind of square. Denote the chemical potentials of the rhombi by μ_1 and μ_2, and let μ_{sq} be the chemical potential of the squares. Without loss of generality, we may assume $\mu_2 \geqslant \mu_1$ and consider the I_0 phase. In Lieb and Wu's notation,[38] the vertex energies are given by

$$\begin{aligned} &e_1 = -\mu_2, \qquad e_4 = -\mu_1 \\ &e_2 + e_3 \to +\infty \\ &e_2 - e_3 = \mu_2 - \mu_1 + \mu_{sq} \\ &e_5 = e_6 = -\mu_{sq}/2 \end{aligned} \tag{53}$$

Here e_2 and e_3 go to infinity because vertices 2 and 3 are disallowed. After some lengthy but otherwise straightforward calculations, one finds that a finite entropy density (*per area*) exists, due to the randomness of the tilings, which is given by

$$\sigma_I = \frac{1}{\sqrt{2}\,\pi}\,[\sqrt{2} + (\sqrt{2}-1)d][tI'(t)\log t - I(t)] \tag{54}$$

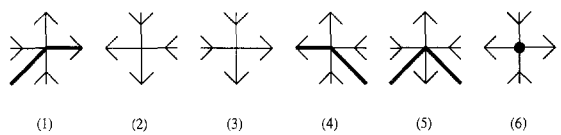

Fig. 7. After lattice distortion, the I_0 phase can be mapped onto a 6-vertex model. Bold line segments, which we show superimposed onto the vertices, form tile edges. The restriction that the assembly of these bold lines form tiles is thus equivalent to the ice rules in the 6-vertex model. Notice that vertices 2 and 3 are disallowed, and vertex 6 only appears at the centers of tilted squares (13). Vertex energies are given in Eq. (53).

where

$$t = \exp(\mu_2 - \mu_1) \tag{55}$$

and

$$I(t) = \frac{1}{2}\int_0^{k_f} \log(1 + t^2 - 2t\cos k)\, dk \tag{56}$$

with $k_f = (\sqrt{2} - d)\pi/[\sqrt{2} + (\sqrt{2} - 1)d]$, and d is the rhombus density, which has to be determined through the following equation:

$$\mu_{sq} - \mu_1 - \mu_2 + \frac{I(t)}{\pi} - \frac{2 + (1 - \sqrt{2})\, d}{2 + (2 - \sqrt{2})d} \log(1 + t^2 - 2t\cos k_f) = 0 \tag{57}$$

A transition between the square phase and the incommensurate phase occurs when $d = 0$. Substituting into Eq. (57), we get the phase boundary

$$\exp(\mu_1) + \exp(\mu_2) = \exp\left(\frac{\mu_{sq}}{2}\right) \tag{58}$$

Near the transition, the domain wall density goes continuously to zero with critical exponent 1/2,

$$d \simeq \frac{\sqrt{2}}{\pi}\left[\exp(-\mu_1) + \exp(-\mu_2)\right]\left[\log \frac{\exp(\mu_{sq}/2)}{\exp(\mu_1) + \exp(\mu_2)}\right]^{1/2} \tag{59}$$

Thus, the transition is continuous. Another transition between the rhombic crystal phase (containing rhombi with chemical potential μ_2) and the incommensurate phase occurs when $d = 1/\sqrt{2}$. Substituting into Eq. (57), we get the phase boundary

$$\exp(\mu_{sq}) + \exp(\mu_1 + \mu_2) = \exp(2\mu_2) \tag{60}$$

Again we can check that density of squares approaches 0 continuously with an exponent 1/2.

Transitions of this type belong to a general universality class known as commensurate–incommensurate (C–IC) or Pokrovsky–Talapov (PT) transitions,[40,41] which are conveniently represented by one-dimensional free fermion models.[40] Fermions can either hop left or right. Thus, in the space-time plane a meandering fermion world line corresponds to a domain wall in our tiling model. Let n_f be the fermion density and μ the chemical potential of the fermion per unit length. Then in the limit of small n_f the leading meandering entropy is $n_f \log 2$, where $\log 2$ appears simply because

fermions can either hop left or right. The next order contribution comes from fermion repulsion, which reduces the total entropy. We now argue that this term is proportional to n_f^3.

Consider an area of size $L_x \times L_y$. The number of fermions passing through this region is $n_f L_x$ and the average distance between neighboring fermions is $1/n_f$. In the limit of small n_f, each fermion is well approximated by a random walker, so that horizontal displacement is the square root of vertical displacement. Then neighboring fermions touch each other roughly after vertical displacement $L_y \simeq 1/n_f^2$. The density of contacts is given by the number of fermions $n_f L_x$ divided by the area $L_x L_y = L_x/n_f^2$ in which we expect them each to collide once on average. The density of contacts thus is cubic in the density of fermions for small densities and we can write the free energy density for the free fermion system as

$$f = -(\log 2 + \mu)\, n_f + q n_f^3 \tag{61}$$

where q is some constant. Minimizing the free energy density with respect to n_f yields the equilibrium value of n_f,

$$n_f = \begin{cases} \left[\dfrac{3a}{\sqrt{2}}(\mu + \log 2)\right]^{1/2} & \text{if} \quad \mu > -\log 2 \\ 0 & \text{if} \quad \mu < -\log 2 \end{cases} \tag{62}$$

Thus, the order parameter exponent is 1/2.

In addition to the connection with two-dimensional C–IC transitions, this exactly solvable limit can be interpreted as a surface roughening model. In view of the importance of higher-dimensional-space description of quasicrystals outlined in Sections 2.2–2.4, this interpretation is especially enlightening. Blöte and Hilhorst[42] showed that a random tiling of the plane by 60° rhombi corresponds to a fluctuating surface of a simple cubic crystal viewed from the [1, 1, 1] axis. A slight deformation (changing 60° angles into either 45° or 90° angles) transforms these 60° rhombus tilings into our exactly solvable tilings. In Blöte and Hilhorst's language, our commensurate square phase corresponds to a perfectly flat surface. Our de Bruijn lines correspond to steps increasing the heights of this surface by one unit. In the stepped phase, the fluctuating surface deviates logarithmically from its average orientation, so that the tilted surface is defined as "rough." It is very easy to define the height variable appropriate for our I_α phase: every domain of square tiles has a constant (integer) height. The relative height of two domains is given by the number of domain walls of type α separating the two domains. This surface roughening transition is C–IC in nature, instead of the more usual Kosterlitz–Thouless transition,

because step meanderings are *anisotropic*. Islands, for instance, are forbidden. The 60° rhombus tiling model appears superficially isotropic because three families of anisotropic domain walls are superposed at 120° angles.

3.3. Construction of the Transfer Matrix

In the quasicrystal phase where all types of tiles are present, no exact solution is known and we have to study this phase numerically using a transfer matrix approach. The transfer matrix technique was first proposed for random tiling models of quasicrystals by Henley,[17] and later was successfully applied to a tiling model by Widom *et al.*[22] In transfer matrix techniques one usually divides the system into layers, and compatibility rules between one layer and its neighbors must be worked out in order to generate the transfer matrix. The lattice version of our model makes the construction of the transfer matrix particularly convenient. The definition of layers is simple: one uses the layer formed by two neighboring rows of lattice sites on the square lattice. The boundary condition we use here is also simple: one cuts off those parts of the tiles that fall outside of the system width, and chemical potentials of these fractional tiles are taken to be proportional to their fractional areas. This corresponds to a "free boundary."

The building blocks of the transfer matrix in our model, which we call "states," are assignments of four-dimensional coordinates to an entire row of lattice sites. The neighboring sites can be connected by bonds in three ways as shown in Figs. 8a–8c. When a lattice site corresponds to the center of a tilted square, the configuration in Fig. 8d must occur. The total number of states, which is the dimension of the transfer matrix, is empirically found to grow exponentially, roughly as 3.3^N, where N is the system width. This prevents us from studying systems of larger widths. A layer is labeled by two indices i and j which correspond to the two rows of lattice sites i and j bounding the layer. The transfer matrix is defined as

$$T_{ij} = \begin{cases} \exp\left(\sum_{\alpha\beta} N_{\alpha\beta}^{(i,j)} \bar{\mu}_{\alpha\beta}\right) & \text{if a layer is formed} \\ 0 & \text{otherwise} \end{cases} \tag{63}$$

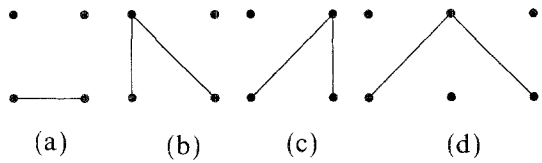

Fig. 8. (a–c) Three possible bond configurations linking neighboring vertices in a row. (d) An empty lattice site, which corresponds to the center of a tilted square.

where $N_{\alpha\beta}^{(i,j)}$ is the number of $(\alpha\beta)$ tiles contained in the layer (i, j). Note that these chemical potentials $\bar{\mu}_{\alpha\beta}$ are defined on the lattice after the distortion, and in our numerical study we have always set $\bar{\mu}_{13}=0$ without loss of generality. Also note that most of the matrix elements are zero because transfer rules are very restrictive. Because the transfer matrix is very sparse, we only store the nonzero elements in the computer in order to save space.

The transfer matrix thus constructed is not symmetric, and we need both the left eigenvector and right eigenvector to calculate various statistical averages. The eigenvalue and eigenvectors are calculated using an iteration method. Tile densities and entropy density are, respectively,

$$\bar{n}_{\alpha\beta}=\frac{1}{N\lambda}\sum_{i,j} l_i T_{ij} N_{\alpha\beta}^{(i,j)} r_j \tag{64}$$

and

$$\bar{\sigma}=\frac{1}{N}\log\lambda-\sum_{\alpha\beta}\bar{n}_{\alpha\beta}\bar{\mu}_{\alpha\beta} \tag{65}$$

where λ denotes the largest eigenvalue and l and r are the left and right eigenvectors corresponding to the largest eigenvalue. Notice that quantities defined above are lattice densities, where we simply divide tile numbers or entropy per row by the lattice width N. Off-lattice densities are

$$d_{\alpha\beta}=\frac{\bar{n}_{\alpha\beta}}{\sum_{\alpha\beta}\bar{n}_{\alpha\beta}a_{\alpha\beta}} \tag{66}$$

and

$$\sigma=\frac{\bar{\sigma}}{\sum_{\alpha\beta}\bar{n}_{\alpha\beta}a_{\alpha\beta}} \tag{67}$$

where $a_{\alpha\beta}$ is the area of the undistorted $(\alpha\beta)$ tile.

Finally, we point out that the "free boundary" we used here is crucial both at the C–IC transitions and inside the quasicrystal phase Q. Park and Widom[43] have recently pointed out that in these domain wall systems periodic boundary conditions force the number of domain walls to be fixed; thus domain wall mismatch exists between the finite systems and infinite system. Such a mismatch prevents domain wall densities from vanishing continuously near C–IC transitions, and forces compositions away from their quasicrystalline (or other incommensurate state) values in finite systems. It also generates different scaling corrections to the free energy which depend on the path taken to the thermodynamic limit, which makes finite-size scaling analysis difficult. These effects are avoided by taking the free boundary condition which allows domain walls to enter or exit at the boundary.[39,44]

3.4. Landau Expansion of Quasicrystal Entropy

The quasicrystal phase in our model can be described by two sets of domain walls running in two different directions. Such walls are also called de Bruijn lines. However, only two sets of de Bruijn lines out of the total of four are necessary to fully describe the quasicrystal phase. In particular, we can choose them to be those walls which connect centers of horizontal and vertical bonds, respectively. In order that qualitative features of our results not be obscured by unnecessary mathematical complexity, we further restrict our discussion to the case

$$\begin{aligned} \mu_{01} &= \mu_{03} \equiv \mu_{\mathrm{H}} \\ \mu_{12} &= \mu_{23} \equiv \mu_{\mathrm{V}} \end{aligned} \tag{68}$$

so that the two types of domain walls go, respectively, vertically and horizontally on average. Correspondingly, we define

$$\begin{aligned} d_{\mathrm{H}} &= d_{01} + d_{03} \\ d_{\mathrm{V}} &= d_{12} + d_{23} \end{aligned} \tag{69}$$

Note that d_{H} and d_{V} are related to type 0 and 2 domain wall densities by a factor of $1/\sqrt{2}$.

Let us focus on the limit of small d_{H} and d_{V}. The entropy density

$$\begin{aligned} &S(N_{13}, N_{02}, N_{01} = N_{03}, N_{12} = N_{23})/A(N_{13}, N_{02}, N_{01} = N_{03}, N_{12} = N_{23}) \\ &\quad \equiv \sigma(d_{\mathrm{H}}, d_{\mathrm{V}}) \end{aligned}$$

depends only on horizontal and vertical rhombus densities d_{H} and d_{V}, due to the imposed symmetry in Eq. (68), the nonlinear constraint (30), and the area relation (4). That is, we can express the densities of squares and tilted squares in terms of d_{H} and d_{V},

$$\begin{aligned} d_{02} &= \frac{1}{2} d_{\mathrm{H}} d_{\mathrm{V}} \\ d_{13} &= 1 - \frac{1}{\sqrt{2}} (d_{\mathrm{H}} + d_{\mathrm{V}}) - \frac{1}{2} d_{\mathrm{H}} d_{\mathrm{V}} \end{aligned} \tag{70}$$

where we have kept terms up to the order $d_{\mathrm{H}} d_{\mathrm{V}}$. The entropy density of the quasicrystal phase can then be written as

$$\sigma_Q(d_{\mathrm{H}}, d_{\mathrm{V}}) = \sigma_I(d_{\mathrm{H}}) + \sigma_I(d_{\mathrm{V}}) - \Phi(d_{\mathrm{H}}, d_{\mathrm{V}}) \tag{71}$$

where d_H and d_V are the densities of tiles with horizontal and vertical bonds, respectively, and $\sigma_I(d)$ is the entropy density of the incommensurate phases given by Eq. (54). Expanding Eq. (54) in the small-d limit, we obtain

$$\sigma_I(d) = d \log 2 - \frac{\pi^2}{24} d^3 + \cdots \tag{72}$$

The term $\Phi(d_H, d_V)$ in Eq. (71) comes from interaction (crossings) between the two types of domain walls. We believe such a term reduces the total entropy because whenever two walls cross there is only one local configuration possible corresponding to a square, while walls that do not cross will not have such a restriction. Symmetry between the two types of walls indicates that $\Phi(d_H, d_V)$ is symmetric about its arguments, and $\Phi(d_H, d_V)$ is zero whenever one of its arguments is zero, since there is no interaction present. Thus the lowest-order term in Φ is of the form $\frac{1}{2}ad_H d_V$ and the next higher-order term can be written in the form $bd_H d_V(d_H + d_V)$, where a and b are constants. In particular, a is expected to be positive, so that the total entropy is reduced due to domain wall crossing.

Choosing the C_{13} phase as a reference in which $d_H = d_V = 0$, we can obtain the free energy density difference between the quasicrystal phase and C_{13} from the entropy density (71) when we take into account the chemical potentials of the squares which replace rhombi at domain wall crossings. We express the density of squares in terms of d_H and d_V through Eq. (70). Then

$$\begin{aligned} f_Q(d_H, d_V, \mu_H, \mu_V) = & -\mu_H d_H - \mu_V d_V - \tfrac{1}{2}(\mu_{02} - \mu_H - \mu_V)\, d_H d_V \\ & - \sigma_Q(d_H, d_V) \end{aligned} \tag{73}$$

Near the multicritical points such as A in Fig. 9, domain wall densities approach zero and the free energy (73) can be expanded into a series in powers of densities,

$$\begin{aligned} f_Q(d_H, d_V, \mu_H, \mu_V) = & -(\mu_H + \log 2)\, d_H + \frac{\pi^2}{24} d_H^3 - (\mu_V + \log 2)\, d_V + \frac{\pi^2}{24} d_V^3 \\ & - \frac{1}{2}(\delta - a)\, d_H d_V + b d_H d_V (d_H + d_V) \end{aligned} \tag{74}$$

where $\delta \equiv \mu_{02} - \mu_H - \mu_V$, and we have expanded $\sigma_Q(d_H, d_V)$ according to Eq. (71). Equation (74) forms the basis of the Landau theory that we shall study in detail in Section 5.

Our view of the quasicrystal phase in terms of two perpendicular

families of domain walls presents a nice generalization of the surface roughening model of Blöte and Hilhorst. Now instead of assigning a single height variable to each domain of tilted squares, as was done in the I_0 phase, we require two independent height variables. The first counts the number of type $\alpha = 0$ walls crossed, while the second counts the number of type $\alpha = 2$ walls crossed. The "roughening" transition from the "flat" C_{13}

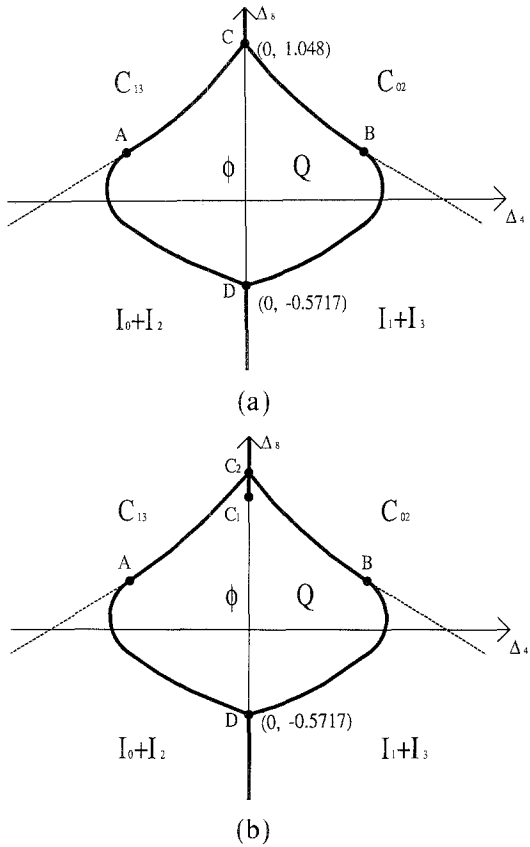

Fig. 9. (a) A cross section of the phase diagram with 4-fold symmetry. The quasicrystal phase region is enclosed by the boundary connecting points A, B, C, and D. Boundaries AC and BC are predicted to be first-order by Landau theory, but numerical determination is difficult. Boundaries AD and BD correspond to first-order phase transitions from $I_0 \oplus I_2$ and $I_1 \oplus I_3$ to the quasicrystal phase, respectively. The precise location has not been determined. The vertical line segment CD corresponds to the strain-free perfect quasicrystal state ϕ. The remainder of the Δ_8 axis are points of first-order transition. Broken lines ending at A and B are locations of C–IC phase transitions between square phases and incommensurate phases and are determined in Eq. (89). (b) The same cross section as in (a), but with the assumption that $C_1 C_2$ corresponds to a region where phason strained quasicrystal states coexist. The length of the line segment $C_1 C_2$ is exaggerated.

phase to the quasicrystal phase Q corresponds to the roughening of a two-dimensional surface into a four-dimensional space instead of the conventional three.

One note of warning is in order: although we combine Landau theory, numerical transfer matrix calculations, and exact solutions to determine the phase diagram, there is always the chance of missing important phases and of incorrectly locating transitions due to finite-size effects in numerical calculations. Also, the existence and analyticity of the Landau expansion in Eq. (74) should also not be taken for granted. Our discussion of the one-dimensional Hubbard model in Section 6.6 sheds some light on these two issues.

4. CROSS SECTIONS OF PHASE DIAGRAM

In this section we shall present various cross sections of our proposed phase diagram, which have 8-fold, 4-fold, and 2-fold rotational symmetries, respectively. As we have already pointed out, the phase diagram is five-dimensional and therefore has five axes. We choose the following combinations of chemical potentials to label the axes of the phase diagram

$$\begin{aligned}
\Delta_8 &= \frac{1}{2}(\mu_{02}+\mu_{13}) - \frac{\sqrt{2}}{4}(\mu_{01}+\mu_{12}+\mu_{23}+\mu_{03}) \\
\Delta_4 &= \mu_{02}-\mu_{13} \\
\Delta_2 &= \frac{1}{2}(\mu_{01}+\mu_{03}-\mu_{12}-\mu_{23}) \\
\Delta_x &= \mu_{03}-\mu_{01} \\
\Delta_y &= \mu_{23}-\mu_{12}
\end{aligned} \tag{75}$$

Along the Δ_8 axis the 8-fold rotational symmetry is maintained except for the spontaneous symmetry breaking. The Δ_4 axis breaks the 8-fold symmetry while still preserving the 4-fold symmetry. Similarly, along the Δ_2 axis the 2-fold symmetry is preserved, and Δ_x and Δ_y maintain the reflection symmetries about the x and y axes (i.e., in $\hat{e}_0^{\parallel}$ and $\hat{e}_2^{\parallel}$ directions), respectively.

4.1. Eight-fold Symmetric Line

We first concentrate on the most symmetric case where the 8-fold rotational symmetry is maintained. This is done explicitly by requiring

$$\begin{aligned}
\mu_{01} &= \mu_{12} = \mu_{23} = \mu_{03} \equiv \mu_{\mathrm{rh}} \\
\mu_{02} &= \mu_{13} \equiv \mu_{\mathrm{sq}}
\end{aligned} \tag{76}$$

Note that there is a constraint between μ_{rh} and μ_{sq} due to the Gibbs–Duhem relation, Eq. (9). Also, all the Δ's defined in Eq. (75) now have zero values except for Δ_8; we then see that Eq. (76) forms a line which lies on the 8-fold symmetric Δ_8 axis.

There are four possible phases on the Δ_8 axis:

1. C_{02} and C_{13} coexist, no rhombi.
2. I_0, I_1, I_2, and I_3 coexist.
3. Phason strained quasicrystal phases coexist.
4. The perfect quasicrystal state ϕ.

These four cases fill up the entire Δ_8 axis. Inside the perfect quasicrystal phase the tile densities and entropy density σ_0 should remain constant,

$$d_{01} = d_{12} = d_{23} = d_{03} = \frac{1}{4\sqrt{2}}$$
$$d_{02} = d_{13} = \frac{1}{4} \tag{77}$$

From Eqs. (48) and (75) we then have

$$\sigma_0 = -\left(\frac{\mu_{rh}}{\sqrt{2}} + \frac{\mu_{sq}}{2}\right) \tag{78}$$

and

$$\Delta_8 = \mu_{sq} - \sqrt{2}\,\mu_{rh} \tag{79}$$

Numerically we have (see Section 4.2 and Table I)

$$\sigma_0 = 0.5240 \pm 0.0005 \tag{80}$$

Entropy at the perfect quasicrystal point has been reported previously in Monte Carlo simulation (ref. 45; results reported in ref. 17), with a value $\sigma_0 = 0.3943$ per tile. This is equivalent to 0.4760 in our units (per area). Thus, a substantial unexplained discrepancy exists.

Figure 9 displays two alternative scenarios along the Δ_8 axis. In both scenarios the system enters the four coexisting incommensurate phases on one side of the perfect quasicrystal state ϕ through a first-order phase transition. The location (point D in Figs. 9a and b) of this first-order phase transition can be determined by combining the exact solution in Section 3.2 and Eq. (78), as described in Eq. (12). This yields $\Delta_8(D) = -0.5717$. Tile densities are discontinuous at point D. This result is supported by numerical data as well as values of phason elastic constants (see Section 6.2 and discussions below).

On the other side, the strain-free quasicrystal state ϕ terminates either at a point C as in Fig. 9a, or in a sequence of transitions at C_1 and C_2 (Fig. 9b) in the vicinity of $\Delta_8 \simeq 1.0$. That is, the system either directly enters $C_{02} \oplus C_{13}$ through a first-order phase transition or goes through an intermediate region of coexisting phason strained quasicrystal states. We shall discuss both cases in the following.

1. Assume that the point C actually corresponds to the boundary between $C_{02} \oplus C_{13}$ and ϕ. Then $\mu_{sq} = 0$ at point C and we have

$$\mu_{rh} = -\sqrt{2}\,\sigma_0 \tag{81}$$

and (see Fig. 9a for point C)

$$\Delta_8(C) = 2\sigma_0 = 1.048 \tag{82}$$

which is rather close to the numerically observed value. The resulting phase diagram is pictured in Fig. 9a.

2. There is another possibility that in between $C_{02} \oplus C_{13}$ and ϕ there exists a small region in which phason strained quasicrystal states coexist. If that is the case, then these states are related by 45° rotations so that the coexisting phase has 8-fold rotational symmetry. Further analysis (see Section 6.2) indicates that each individual state has 4-fold symmetry and we only need two such states (related by a 45° rotation) to coexist. This coexisting phase then further transforms into $C_{02} \oplus C_{13}$ via a first-order transition. Figure 9b describes such a possibility.

Numerical study has been unable to determine which case is correct, due to finite-size effects in our transfer matrix calculations. But it gives an upper bound on the location of C_1 (Fig. 9b): $\Delta_8(C_1) \leqslant 1.099$. Thus, points C and C_1 are rather close, if they are distinct. Section 6.2 discusses this issue in more detail. In the rest of this paper we shall present cross sections of the phase diagram according to the first case, although recent experimental results on the phase diagram of icosahedral AlCuFe, reported by Bancel,[46] may be better explained in terms of Fig. 9b. Thus, we should keep in mind that either scenario is possible in principle.

It is interesting to note that the 8-fold symmetric quasicrystal states occupy a finite interval along the Δ_8 axis. This is expected in view of the quadratic constraint, Eq. (30). The precise mechanism is quite interesting. Consider the states with 8-fold symmetry (i.e., $d_{01} = d_{12} = d_{23} = d_{03}$ and $d_{02} = d_{13}$) encountered along the Δ_8 axis in Fig. 9. The relationships between phason strains and tile densities, Eq. (28), demand that $\mathsf{E} = 0$ in the presence of 8-fold rotational symmetry among tile densities. But for

$E = 0$ the densities have the unique values given by Eq. (77). Thus the variable conjugate to Δ_8,

$$d_8 = \frac{d_{02} + d_{13}}{2} - \frac{1}{2\sqrt{2}}(d_{01} + d_{12} + d_{23} + d_{03}) \tag{83}$$

vanishes. Of course, it is possible to force, in the canonical ensemble, the value of d_8 to take any value between $-1/2$ and $+1/2$.

Such states with $d_8 \neq 0$ must violate Eq. (28). That is, they cannot be described by a uniform phason strain, and they must lack the approxi-

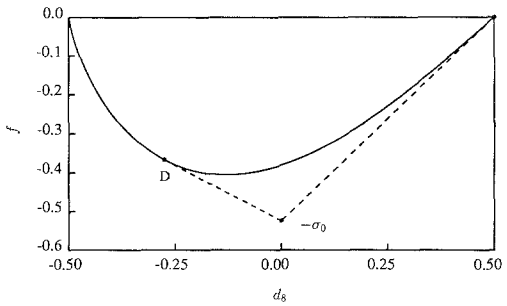

(a)

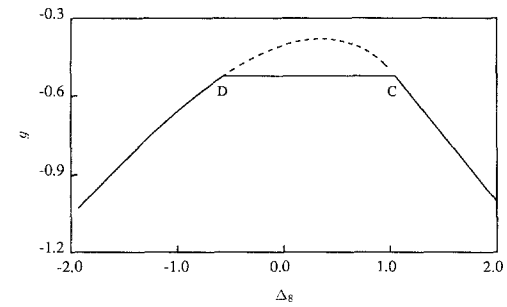

(b)

Fig. 10. (a) Helmholtz free energy $f = -\sigma_I$ for $d_8 \neq 0$, and $= -\sigma_0$ for $d_8 = 0$; the dashed lines are obtained from the Maxwell construction, whose slopes determine the values of the chemical potentials at the phase transitions. (b) The Legendre transform of (a). The curve to the left of D corresponds to the incommensurate phase, whose analytical continuation is denoted by the dashed curve, which is unstable. DC is the locked quasicrystal state ϕ and the line to the right of C corresponds to the square phase.

mating plane defined in Eq. (22), whose existence allows for Eq. (28). Very likely the proper description is in terms of coexisting incommensurate phases I_α or $C_{02} \oplus C_{13}$ as we already suggested in this section (the possibility of phason strained quasicrystal states coexisting is discussed in Section 6.2). Since all four incommensurate phases are equivalent to one another, the Helmholtz free energy density for the coexisting phase is identical to the free energy density of any one of them,

$$f(d_8) = -\sigma_I(d_{\text{rh}}) \tag{84}$$

as is drawn in Fig. 10a, where d_{rh} is the rhombus density in the incommensurate phase. When d_8 is precisely equal to zero there is an additional state possible, the quasicrystal with entropy density $\sigma_0 > \sigma_I$.

Legendre-transforming to the field variable Δ_8 conjugate to d_8, one then obtains Fig. 10b,

$$g(\Delta_8) = \min_{d_8} (f - \Delta_8 d_8) \tag{85}$$

consisting of one smooth arc when the equilibrium state is the coexisting I_α phase, and two line segments corresponding to locking on the quasicrystal and square phases. Legendre-transforming back yields the free energy function shown in dashed lines in Fig. 10a. Kinks in free energy curves, such as seen in Fig. 10a at $d_8 = 0$, have been previously related to locking on quasicrystal concentrations by Burkov.[47] The slope of the solid curve in Fig. 10a at $d_8 = 1/2$ can be calculated exactly, using the exact solution in Section 3.2, and is equal to $\sqrt{2} \log 2$. The slope of the dashed line is $2\sigma_0$. Thus, the near tangency at $d_8 = 1/2$ provides a close lower bound $\sigma_0 \geqslant (1/\sqrt{2}) \log 2 = 0.4901$. This is consistent with the value in Eq. (80), but inconsistent with Orrick's result.[45]

We comment in passing that the phenomenon of locking onto the perfect quasicrystal state ϕ provides an interesting and rare example of the so-called "anomalous first-order transitions,"[48] at which the volume stays constant while pressure (our Δ_8) undergoes a jump. Anomalous first-order transitions are known to occur in systems with sufficiently strong many-body interactions,[48] and are related to the incompressible fluid states in the fractional quantized Hall effect,[49,50] and to the "superconducting" phase in the 1D Hubbard model (see Section 6.6).

Although we focused our attention on locking on the quasicrystal state with 8-fold symmetry, it is important to note that the locking is more general. In fact, throughout the quasicrystal phase there exist lines relating Δ_x, Δ_y, Δ_2, Δ_4, and Δ_8 along which the state remains invariant until a phase transition takes place at some particular point,

$$
\begin{aligned}
\Delta_x &= \Delta_x^0 + (d_{12} - d_{23})t \\
\Delta_y &= \Delta_y^0 + (d_{01} - d_{03})t \\
\Delta_2 &= \Delta_2^0 + \tfrac{1}{2}(d_{12} + d_{23} - d_{01} - d_{03})t \\
\Delta_4 &= \Delta_4^0 + (d_{02} - d_{13})t \\
\Delta_8 &= \Delta_8^0 - \left[\frac{d_{02} + d_{13}}{2} + \frac{\sqrt{2}}{4}(d_{01} + d_{12} + d_{23} + d_{03})\right] t
\end{aligned}
\tag{86}
$$

for t a real parameter. This follows because of the existence of the nonlinear constraint, Eq. (30), and implies that only four independent variables are required to specify a thermodynamic state within the phason strained quasicrystal phase. Locking on the symmetric quasicrystal state is just a special case of Eq. (86) with $\Delta_x^0 = \Delta_y^0 = \Delta_2^0 = \Delta_4^0 = 0$. We choose to explore the five-dimensional phase diagram instead of a four-dimensional one because outside the quasicrystal phase, in the incommensurate and crystal phases, the nonlinear constraint, Eq. (30), becomes the area constraint, Eq. (29).

Since the chemical potentials for tiles should depend on temperature, pressure, and perhaps atomic concentration, one expects to obtain symmetric phason-strain-free quasicrystal states over ranges of these variables. This fact seems to be well supported by experiments. Quasicrystalline materials are usually obtained by cooling, and there seems to be a wide temperature range over which one obtains quasicrystals with perfect rotational symmetries. In other words, we do not have to fine tune the temperature or pressure. The fact that quasicrystals often exist over ranges of atomic concentration is surely due to the possibility of substitutional disorder or vacancy formation, effects not included in tiling models except through the variation of tile chemical potentials.

4.2. Four-fold Symmetric Planes

We now proceed to expand the phase diagram obtained in the previous subsection by adding one axis, which breaks the 8-fold symmetry, but preserves the 4-fold symmetry. There are actually two ways to do this, yielding two different cross sections of the phase diagram. We first consider the case in which the symmetry among the rhombi is preserved, but the symmetry between the two types of squares is broken (this breaks the symmetry of the "between" mirror plane[51])

$$
\begin{aligned}
&\mu_{01} = \mu_{12} = \mu_{23} = \mu_{03} \equiv \mu_{\mathrm{rh}} \\
&\Delta_4 = \mu_{02} - \mu_{13}
\end{aligned}
\tag{87}
$$

Figure 9a shows the phase diagram in such a cross section with the assumption that coexisting phason strained quasicrystal states do not appear. It is symmetric about the Δ_8 axis. Positive values of Δ_4 favor regular squares, so that $C_{02} \oplus C_{13}$ and $I_0 \oplus I_1 \oplus I_2 \oplus I_3$ break down to C_{02} and $I_1 \oplus I_3$, respectively, on the right-hand side of the Δ_8 axis. The region Q represents the quasicrystal phase. Nonzero values of Δ_4 generate phason strains. The two straight dashed lines ending at points A and B, respectively, are two transition lines, along which C–IC phase transitions take place between commensurate square phases and incommensurate I phases. These two lines can be determined by using the exact solutions of the incommensurate phases we obtained previously. Since chemical potentials of the rhombi are all equal, Eq. (58) yields

$$\mu_{\mathrm{rh}} = -\log 2 \tag{88}$$

Note that $\mu_{02} = 0$ in the C_{02} phase and $\mu_{13} = 0$ in the C_{13} phase. We then immediately see that the two transition lines are

$$\Delta_8 = \pm \tfrac{1}{2}\Delta_4 + \sqrt{2} \log 2 \tag{89}$$

Curve ADB represents transitions from the quasicrystal phase to $I_0 \oplus I_2$ or $I_1 \oplus I_3$. As we have argued previously in Section 3.1, these are in general first-order transitions. It is only at points A and B, where Q and these incommensurate phases continuously change to the square phases, that we get continuous phase transitions. Thus, points A and B correspond to two multicritical points. Numerically we have identified

$$\Delta_8(A, B) = 0.56 \pm 0.03 \tag{90}$$

Curves AC and BC are transition lines separating the quasicrystal phase from the square phases. These transitions are in general first order, except at points A and B, where latent heat vanishes. This is suggested by Landau theory (see Section 5) and also well supported by numerical calculations (Fig. 19a). Note that AC and BC meet in a "kink." Adopting the Clapeyron equation to our tiling model[34] shows the slopes of these phase boundaries are ± 1. Similarly, AD and BD also meet in a "kink."

We can scan across the Δ_8 axis and compute the entropy density. According to Elser and Henley's hypothesis, we should expect to see the entropy maximum on the Δ_8 axis if we stay inside the quasicrystal phase. Figure 11 shows entropy densities as we cross the Δ_8 axis following the paths $\mu_{02} + \mu_{13} - 3\mu_{\mathrm{rh}} = -0.5$, 0, 0.5, 1, which intersect with the Δ_8 axis at $\Delta_8 = -0.2735$, -0.0309, 0.2118, 0.4544. In all four cases the maximum entropy points fall at $\Delta_4 = 0$. Furthermore, they all share the same maxi-

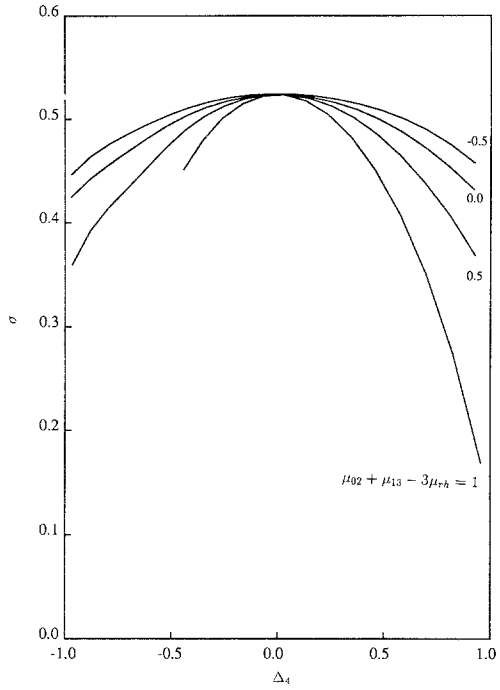

Fig. 11. The entropy densities (per area) as we go across the *CD* line (see Fig. 9) following the curve $\mu_{02}+\mu_{13}-3\mu_{\rm rh}=-0.5, 0, 0.5, 1$. In all these cases, the entropy maximum occurs at $\Delta_4=0$. Furthermore, it always has the same value.

mum entropy density. Newton's algorithm was used to search for the entropy density maximum points for various finite-size systems in this subspace. Table I lists various tile densities at maximum entropy points for different finite-size systems as a result of such a search. After extrapolation we get $\Delta_4=-0.0008\pm0.0009$ and $\sigma_0=0.5240\pm0.0005$. As expected, the extreme is indeed at $\Delta_4=0$. Note also that Eq. (51) is nicely satisfied.

Another 4-fold symmetric plane can be obtained when we restrict ourselves to the subspace (which breaks the symmetry of the "along" mirror plane[51])

$$\begin{aligned}\Delta_x&=-\Delta_y\equiv\Delta_4'\\ \Delta_4&=0\\ \Delta_2&=0\end{aligned}\tag{91}$$

Note that the four incommensurate phases are always degenerate, an indication of the 4-fold rotational symmetry. Also, C_{02} and C_{13} always

Table I. Chemical Potentials and Tile Densities at Maximum Entropy Density Points for Finite Systems[a]

	$N=3$	$N=4$	$N=5$	$N=6$	$N=7$	$N=8$	$N=\infty$
$\bar{\mu}_{rh}$	-0.2215	-0.1920	-0.1745	-0.1629	-0.1547	-0.1487	-0.1086 ± 0.0002[b]
$\bar{\mu}_{02}$	-0.5348	-0.4634	-0.4211	-0.3932	-0.3735	-0.3589	-0.2622 ± 0.0002[b]
d_H	0.5313	0.5011	0.4790	0.4620	0.4487	0.4381	0.348 ± 0.004
d_V	0.3071	0.3113	0.3154	0.3194	0.3229	0.3259	0.357 ± 0.004
d_{02}	0.1379	0.1557	0.1692	0.1796	0.1878	0.1944	0.2506 ± 0.0006
d_{13}	0.2693	0.2699	0.2690	0.2679	0.2666	0.2654	0.251 ± 0.001
ψ	0.5347	0.4633	0.4210	0.3932	0.3735	0.3588	0.2621 ± 0.0005[b]
σ_0	1.0695	0.9267	0.8421	0.7864	0.7470	0.7177	0.5240 ± 0.0005[b]

[a] Newton's algorithm is used in a restricted space defined in Eq. (87) to search for maximum entropy points. Extrapolation results are obtained by fitting to Eq. (124), unless otherwise specified. d_H and d_V are defined in Eq. (69). Note that the value $\Delta_4 = \bar{\mu}_{02} + \psi$ is -0.0001 ± 0.0007, which is essentially zero. The extrapolated results agree with Eqs. (77) and (51).

[b] Using θ-algorithm.

coexist. Figure 12 shows this cross section of the phase diagram. Two broken curves ending at E and F are critical lines representing C–IC phase transitions. However, unlike Eq. (89), they are no longer straight, because in general the two kinds of rhombi in the same I phase do not have the same chemical potentials. Considering that $\mu_{sq} = 0$ everywhere inside $C_{02} \oplus C_{13}$, and combining Eq. (58), this critical curve obeys

$$\begin{aligned} \Delta_8 &= -\frac{\sqrt{2}}{2}(\mu_a + \mu_b) \\ \Delta_4' &= \mu_a - \mu_b \\ 1 &= \exp(\mu_a) + \exp(\mu_b) \end{aligned} \tag{92}$$

When $\Delta_4' = 0$, Δ_8 in Eq. (92) reaches its minimum value $\sqrt{2}\log 2 = 0.980 < \Delta_8(C)$; thus, the transition line in Eq. (92) never reaches the Δ_8 axis. It is preempted at points E and F, where first-order transitions into the quasicrystal phase take place. As is obvious from the previous discussion of the phase diagram in Fig. 9, curves ECF and EDF are both first-order lines. The Clapeyron equation[34] shows ECF and EDF cross the Δ_8 axis with zero slopes, in contrast to the curves ACB and ADB in Fig. 9.

As we further increase the value of Δ_4', the four I phases eventually

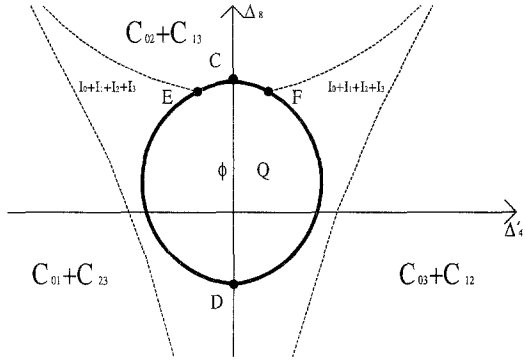

Fig. 12. Another 4-fold symmetric plane. Phase boundaries *CED* and *CFD* are first-order transition lines, but have not been numerically determined. *E* and *F* are points where seven phases meet simultaneously. The quasicrystal phase *Q* is enclosed by *I* phases and squares phases. Broken lines ending at *E* and *F* are locations of C–IC transitions between square phases and four coexisting incommensurate phases and are determined in Eq. (92). Further transition lines between the coexisting commensurate phases and coexisting rhombic phases are determined in Eq. (93).

transform into $C_{03} \oplus C_{12}$ through a continuous transition which belongs to the C–IC type. The phase boundaries can be determined exactly through Eq. (60), by noticing the fact that the chemical potentials of the rhombi forming the rhombic crystals are zero,

$$\Delta_8 = \log[1 - \exp(\pm \Delta'_4)] \mp \frac{\sqrt{2}}{2} \Delta'_4 \tag{93}$$

Points *E* and *F* are quite remarkable because seven phases meet there simultaneously. Because our full phase diagram is five-dimensional, arguments such as the Gibbs phase rule might be used to exclude the possibility of such multiphase points, as the requirement that seven phases meet simultaneously would certainly seem to constitute six constraints, more than the dimensionality of the full phase diagram. However, this is not the case here. These phases in our model are not completely independent from each other. Symmetry relations exist, as are shown in Eq. (52), which make one of the constraints derivable from the other five constraints. Thus, points *E* and *F* have zero dimensions and are truly isolated points in our phase diagram.

Finally, we merely point out that Fig. 12 can be modified in the same way as we did in Fig. 9b to take into account of the possibility of phason strained quasicrystal states coexisting.

4.3. Two-fold Symmetric Planes

There are two ways to obtain 2-fold symmetric planes containing the 8-fold symmetric line,

$$\Delta_x = \Delta_y = 0 \qquad \text{and} \qquad \Delta_4 = 0 \tag{94}$$

and

$$\Delta_x = \Delta_y \qquad \text{and} \qquad \Delta_2 = \Delta_4 = 0 \tag{95}$$

Note that these two cases are related by a 45° rotation and thus are equivalent. We shall only consider the first case. Figure 13 shows such a cross section of the phase diagram. *GCH* is a first-order line along which the square phase $C_{02} \oplus C_{13}$ coexist, with the quasicrystal phase. The two thick straight lines ending at G and H, respectively, are points of C–IC transitions from square phases to incommensurate phases, and satisfy $\mu_{02} = \mu_{13} = 0$, so that

$$\Delta_8 = \pm \frac{\sqrt{2}}{2} \Delta_2 + \sqrt{2} \log 2 \tag{96}$$

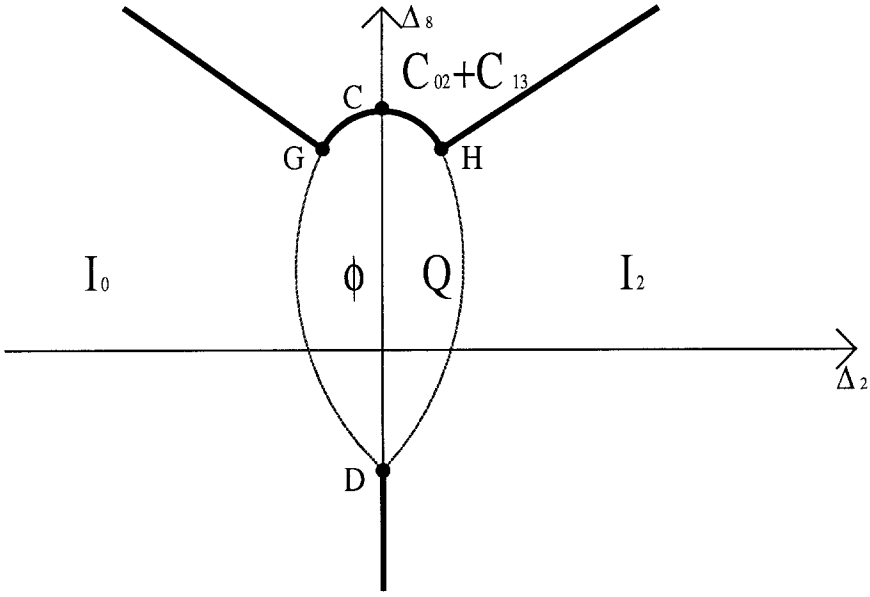

Fig. 13. A 2-fold symmetric plane. Thick curve *GCH* is a first-order transition line which has not been numerically determined. Two thick straight lines ending at G and H are first-order transitions lines, which also coincide with C–IC transition lines between C_{13} and I_0 (or I_2), determined in Eq. (96).

Again these two lines are preempted by the quasicrystal phase, so that they do not reach the Δ_8 axis. The Clapeyron equation[34] shows that GCH crosses the Δ_8 axis with zero slope, while GD and HD meet on the Δ_8 axis with finite slopes.

We point out that the value of perfect quasicrystal entropy in Eq. (80) is crucial. Had we used the value reported in ref. 45, the position of point C would have been lower than $\Delta_8 = \sqrt{2}\log 2$. In that case we can be certain that there is a phase coexisting region between ϕ and $C_{02} \oplus C_{13}$.

5. MULTICRITICAL POINTS

In this section we study more closely the properties of the multicritical points A and B. They share the common property that square phases, incommensurate phases I_α ($\alpha = 0, 1, 2, 3$), and the quasicrystal phase can transform into one another continuously at these points. We shall first examine cross sections of the phase diagram containing the multicritical points deduced from numerical transfer matrix studies. Then the Landau theory proposed in Section 3.4 is studied in more detail. We compare this Landau theory with results from transfer matrix calculations. The similarity between our Landau theory and the classical theory of bicritical, tricritical, and tetracritical points is examined.

5.1. Cross Section of Phase Diagram Containing Multicritical Points

Let us consider planes in the phase diagram parallel to the Δ_4 axis, but perpendicular to the Δ_8 axis, passing through points A and B. There are two inequivalent orientations that are particularly important. We discuss these two cases separately.

First we study the case

$$\begin{aligned} \Delta_4 &= \mu_{02} - \mu_{13} \\ \Delta_8 &= \Delta_8(A) \\ \Delta_2 &= 0 \\ \Delta_x &= -\Delta_y \equiv \Delta \end{aligned} \tag{97}$$

Figure 14 shows the phase diagram in this plane. Points A and B are the two multicritical points. Extreme values of Δ favor rhombic crystal phases. Positive Δ leads to $C_{03} \oplus C_{12}$ coexistence, while negative Δ leads to $C_{01} \oplus C_{23}$. Moderate Δ leads to coexisting incommensurate phases. Positive Δ_4 favors $I_1 \oplus I_3$, while negative Δ_4 favors $I_0 \oplus I_2$. Just as in

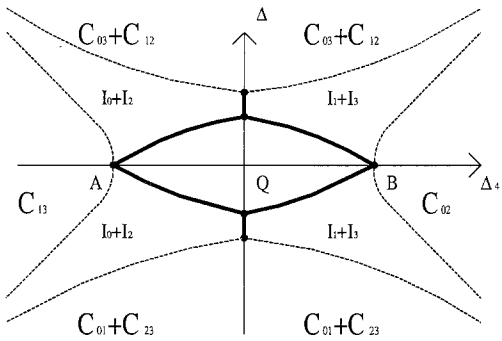

Fig. 14. A plane perpendicular to the Δ_8 axis, passing through the two multicritical points A and B in Fig. 9. As in previous figures, thick curves connecting A and B are first-order lines which have not been numerically determined. The transition becomes continuous at points A and B. Broken curves passing through A and B are C–IC transitions between square phases and incommensurate phases, determined in Eq. (98). The other two broken curves are C–IC transitions between incommensurate phases and rhombic phases, and are determined in Eq. (99).

Fig. 12, the phase boundaries between the rhombic crystal phases and incommensurate phases can be worked out exactly,

$$\begin{aligned} +\Delta_4 &= 2\Delta_8(A) \pm \sqrt{2} - 2\log[1 - \exp(\mp\Delta)] \\ -\Delta_4 &= 2\Delta_8(A) \pm \sqrt{2} - 2\log[1 - \exp(\mp\Delta)] \end{aligned} \tag{98}$$

Extreme values of Δ_4 favor C_{02} or C_{13} depending on the sign of Δ_4. Phase transitions between these square phases and the incommensurate phases occur on [again using Eq. (58)]

$$\begin{aligned} \Delta_4 &= \pm[2\Delta_8(A) + \sqrt{2}\,(\mu_a + \mu_b)] \\ \Delta &= \mu_a - \mu_b \\ 1 &= \exp(\mu_a) + \exp(\mu_b) \end{aligned} \tag{99}$$

Small Δ and Δ_4 lead to the quasicrystal phase Q. The boundary between Q and the incommensurate phase is first order in Landau theory (see Section 6.5). Close to the multicritical points the boundaries have finite slope and vanishing latent heat. Numerical study near those regions is difficult because tile densities are so small that the bulk values are of the same order of magnitude as the finite-size effects.

Next we consider the case

$$\begin{aligned} \Delta_4 &= \mu_{02} - \mu_{13} \\ \Delta_8 &= \Delta_8(A) \\ \Delta_x &= \Delta_y = 0 \\ \Delta_2 &= \mu_{01} - \mu_{12} \end{aligned} \tag{100}$$

which is equivalent to letting

$$\begin{aligned} \Delta_4 &= \mu_{02} - \mu_{13} \\ \Delta_8 &= \Delta_8(A) \\ \Delta_x &= \Delta_y \equiv \Delta \\ \Delta_2 &= 0 \end{aligned} \tag{101}$$

We concentrate on the plane in Eq. (100). Figure 15 shows the phase diagram in this plane. Note that I_1 and I_3 are always degenerate under such parametrization. As in Eq. (99), we have transition lines passing through A and B. In this case they are straight lines

$$\begin{aligned} +\Delta_4 &= 2\Delta_8(A) - 2\sqrt{2}\log 2 \pm \sqrt{2}\,\Delta_2 \\ -\Delta_4 &= 2\Delta_8(A) - 2\sqrt{2}\log 2 \pm \sqrt{2}\,\Delta_2 \end{aligned} \tag{102}$$

The two first-order lines MN and JK are results of competition between rhombi and squares and can be computed numerically by using the exact solution obtained in Section 3.2, in a way described by Eq. (12). These two transition lines preempt the C–IC transitions between $I_1 \oplus I_3$ and rhombic crystal phases for finite values of Δ_2.

5.2. Landau Theory of Multicritical Points

We now analyze in detail the phase diagram near the multicritical point A. Figure 16 shows four possible topologies. We will see that the value of $\delta \equiv \mu_{02} - \mu_{\mathrm{H}} - \mu_{\mathrm{V}}$ determines which topology occurs.

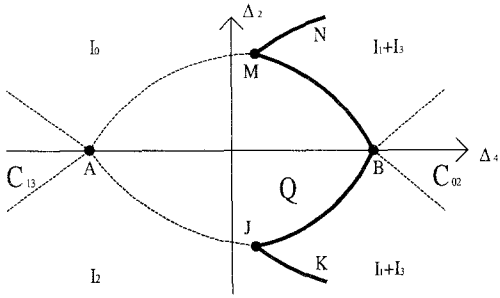

Fig. 15. Another plane perpendicular to the Δ_8 axis, passing through points A and B. Broken curves AM and AJ are continuous transitions according to numerical data. Thick curves BM, BJ, MN, and JK are lines of first-order transitions. The locations of these phase boundaries are not numerically determined. Broken lines ending at A and B are C–IC transition lines determined in Eq. (102).

We seek expressions $d_H(\mu_H, \mu_V)$ and $d_V(\mu_H, \mu_V)$ which can be obtained by minimizing the free energy with respect to d_H and d_V at fixed chemical potentials. Taking derivatives of Eq. (74) with respect to d_H and d_V yields

$$-\tilde{\mu}_H + \frac{\pi^2}{8} d_H^2 - \frac{1}{2}(\delta - a) d_V + b(d_V^2 + 2d_H d_V) = 0 \tag{103}$$

$$-\tilde{\mu}_V + \frac{\pi^2}{8} d_V^2 - \frac{1}{2}(\delta - a) d_H + b(d_H^2 + 2d_V d_H) = 0 \tag{104}$$

where for simplicity we have used $\tilde{\mu}_{H,V} \equiv \mu_{H,V} + \log 2$.

Let us first look at a simple case in which $\tilde{\mu}_H = \tilde{\mu}_V \equiv \tilde{\mu}$. Then $d_H = d_V \equiv d$ simply by symmetry, unless the symmetry is spontaneously broken and we instead have phase coexistence $I_0 \oplus I_2$. Equations (103) and (104) become identical and we get a quadratic equation for d,

$$\left(\frac{\pi^2}{8} + 3b\right) d^2 - \frac{1}{2}(\delta - a) d - \tilde{\mu} = 0 \tag{105}$$

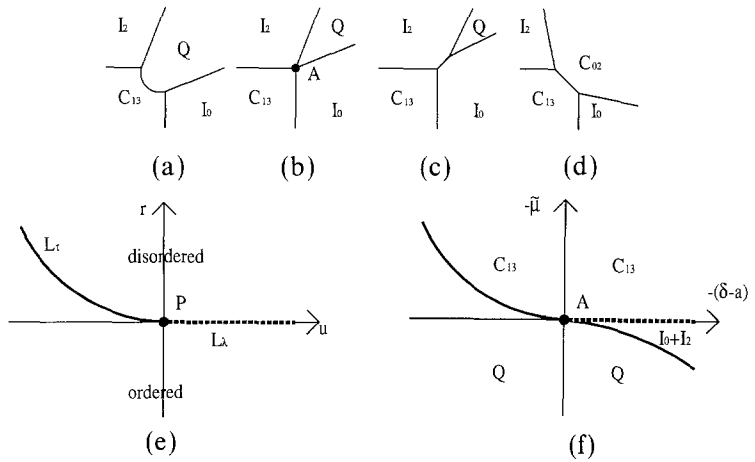

Fig. 16. Phase diagrams near the multicritical point A. (a) At moderate positive values of $\delta - a$ a first-order phase transition happens between C_{13} and Q. (b) At some particular value $\delta = a = 0.55 \pm 0.05$, a continuous transition takes place between C_{13} and Q. (c) When $\delta - a < 0$ there is an I_0 and I_2 coexistence region. (d) When $\delta - a$ is sufficiently large, the quasicrystal phase gets squeezed out by the C_{02} phase. (e) Phase diagram near the tricritical point in the symmetric plane (taken from Fig. 21 of ref. 55). In the disordered phase the order parameter $\psi = 0$, while the ordered region corresponds to the coexistence of two phases with $\psi = \psi_{\pm}$. Here L_τ is a first-order line, while L_λ is continuous. The point P is the tricritical point. (f) The phase diagram of our tiling model in the plane spanned by $-\tilde{\mu}$ and $-(\delta - a)$. The point A is the multicritical point in (b). The transitions between C_{13} and Q, and $I_0 \oplus I_2$ and Q, are first order, except at point A. The transition between C_{13} and $I_0 \oplus I_2$ is continuous (C–IC).

which has two solutions

$$d_{\pm} = 2\left\lceil \frac{\delta - a \pm [(\delta - a)^2 + 2\tilde{\mu}(\pi^2 + 24b)]^{1/2}}{\pi^2 + 24b} \right\rceil \tag{106}$$

We now discuss these two solutions with the assumption that b is sufficiently small so that $\pi^2 + 24b > 0$, which is numerically confirmed in Section 5.3. We discuss separately the cases of $\delta - a$ positive and negative.

First the $\delta - a > 0$ case. In the region where $\tilde{\mu}$ is positive we can only take the plus solution because $d_- < 0$. However, when $\tilde{\mu}$ is negative the minus solution is also possible. Stability analysis is necessary to determine which solution of Eq. (106) is the physically relevant one. The difference between the free energies corresponding to these two solutions is

$$F_+ - F_- = -\frac{8}{3(\pi^2 + 24b)^2}[(\delta - a)^2 + 2\tilde{\mu}(\pi^2 + 24\mathrm{b})]^{3/2}$$

which is always negative. Thus we always take the plus solution. The free energy of this phase is

$$F_+ = -\frac{4}{3(\pi^2 + 24b)^2}[\Delta^3 + (\delta - a)^3 + 3\tilde{\mu}(\delta - a)(\pi^2 + 24b)] \tag{107}$$

where $\Delta^2 = (\delta - a)^2 + 2\tilde{\mu}(\pi^2 + 24b)$. Note that when $\tilde{\mu} = 0$,

$$F_+ = -\frac{8}{3(\pi^2 + 24b)^2}(\delta - a)^3 < 0$$

which means the quasicrystal phase is more stable there, since C_{13}, I_0, and I_2 phases all have vanishing free energies.

The exact phase boundary between the quasicrystal phase and C_{13} obeys $F_+ = 0$, which yields

$$\tilde{\mu} = -\frac{3}{8}\frac{(\delta - a)^2}{\pi^2 + 24b} \tag{108}$$

This is always negative if b is sufficiently small, yielding the picture shown in Fig. 16a. On the quasicrystal side of the phase boundary the value of d is equal to $d = 4(\delta - a)/(\pi^2 + 24b)$, so the tile density is discontinuous and the corresponding phase transition is first order. It is only when $\delta = a$ that this phase transition becomes continuous, which corresponds to the case in Fig. 16b.

Next the $\delta - a < 0$ case. From Eq. (106) only the plus solution is allowed. Furthermore, $\tilde{\mu}$ must be positive in order for d_+ to be positive. However, near $\tilde{\mu} = 0$, the F_+ phase is unstable since F_+ is positive. The

most stable phase corresponds to I_0 or I_2. Thus we have a region in which the I_0 and I_2 phases coexist, which corresponds to the case shown in Fig. 16c. The length of this coexistence line is determined by equating $F_+(\tilde{\mu}) = F_H(\tilde{\mu})$, and a solution is found to have the form $\tilde{\mu} \propto (\delta - a)^2$ in the limit when $\delta - a$ is small. We already know from the discussion in Section 3.1 that such a transition from $I_0 \oplus I_2$ coexistence to the quasicrystal phase is first order.

Finally we point out that when $\delta - a$ is sufficiently large, the Landau expansion is no longer valid. In that case the quasicrystal phase gets squeezed out by the square phase C_{02} and we have a first-order phase transition directly from C_{13} to C_{02}, which is shown in Fig. 16d.

The situation we have described above is rather similar to that in some uniaxially anisotropic antiferromagnetic spin systems which were studied by Fisher *et al.*[52–54] There, at low temperatures, two types of ordered phases exist: in weak magnetic field (parallel to the anisotropy axis) the state is antiferromagnetic with spins parallel or antiparallel to an axis characterizing the anisotropy. In strong magnetic field there is a "spin-flopped" phase in which spins are mostly aligned perpendicular to the axis. A first-order line exists between these two ordered phases, which ends at a "bicritical point" where these two phases become identical to the totally disordered paramagnetic phase. Landau theory[54] further suggests the possible existence of an intermediate phase which exhibits both kinds of order. As a result there exists a "tetracritical point" where the antiferromagnetic phase, spin-flopped phase, and the intermediate phase continuously transform into the paramagnetic phase. In our model I_0 and I_2 are analogues of the two phases with spins aligned parallel and perpendicular to the axis, respectively. The quasicrystal phase corresponds to the intermediate phase because it has both horizontal and vertical rhombi. The C_{13} phase resembles the paramagnetic phase because both have higher symmetries. Thus, in our model a bicritical point occurs when $\delta - a < 0$ (Fig. 16c) and point A in Fig. 16b is actually a tetracritical point. However, in Fig. 16b the two critical lines approach the bicritical point at a right angle, which is rather different from the usual cases in which the two critical lines approach the bicritical point tangentially.[48] This is certainly due to the fact that the critical lines in Fig. 16b represent C–IC transitions. At one side of the transition the system is completely locked into a commensurate phase without any fluctuations, which are known to be responsible for the tangential behavior in the spin-flop transitions. Similarly, we believe our Landau theory reproduces the *exact* behavior at the bicritical point, while the Landau theory of the spin-flop transition[54] *incorrectly* predicts a finite angle between the phase boundaries because of its neglect of fluctuations.

The first-order transition between C_{13} and Q in Fig. 16a distinguishes our model from the usual bicritical/tetracritical behavior because of the absence of a quadratic term $(d_H^2 + d_V^2)$ in the Landau expansion of free energy, Eq. (74). Consider now the case $d_H = d_V \equiv d$ and represent d by ψ^2. It is intriguing to compare our phase diagram near the point A with the phase diagram near a tricritical point in the symmetric plane (see ref. 55 for a review). Following the notations of ref. 55, the free energy in the absence of symmetry-breaking fields is $(r/2)\psi^2 + (u/4!)\psi^4 + (v/6!)\psi^6$. The coefficients u and r vanish at a tricritical point just as the coefficients $-(\delta - a)$ and $-\tilde{\mu}$ in the Landau free energy, Eq. (74), vanish at the multicritical point A in Fig. 16b. Figure 16e shows a typical phase diagram near a tricritical point in the absence of symmetry-breaking fields,[55] while Fig. 16f shows the phase diagram of our tiling model in the space spanned by $-\tilde{\mu}$ and $-(\delta - a)$. The triple line L_τ in Fig. 16e corresponds to the two-phase coexistence line between C_{13} and Q in Fig. 16f. The continuous transition line L_λ in Fig. 16e corresponds to the C–IC transition between C_{13} and $I_0 \oplus I_2$ in Fig. 16f. Note that the shape of the boundaries and the critical exponent are the same in both cases. However, since our model is a two-component system, there is one more transition between $I_0 \oplus I_2$ and Q in Fig. 16f.

5.3. Numerical Study

In this subsection we compare Landau theory with numerical data from the transfer matrix calculation. Such a comparison is rather difficult because in the vicinity of the multicritical points such as A, domain wall densities have rather small values that are of the same order of magnitude as, or even smaller than, the finite-size effects. To overcome this difficulty, we have to rely on good extrapolation techniques and, wherever possible, choose suitable parameters where Landau theory is easier to test.

Our transfer matrix calculation is controlled by the set of on-lattice chemical potentials $\bar{\mu}$'s, which will have to be transformed to μ's according to Eq. (46). However, in the vicinity of the multicritical point A, the shift is $\psi \propto \tilde{\mu}^{3/2}$, which can be obtained from Eq. (107) by letting $\delta = a$. We are concerned with $O(\mu)$ effects which govern the slopes of phase boundaries and phase diagram topology in the vicinity of A. Thus, in this region the phase diagram in the $\mu_{\alpha\beta}$ space has a structure similar to that in $\bar{\mu}_{\alpha\beta}$. In this subsection we only use on-lattice chemical potentials.

Figures 17–19 show numerical evidence supporting the Landau theory phase diagrams in Fig. 16. Figures 17 and 18 are obtained at $\delta = \bar{\mu}_{02} - \bar{\mu}_H - \bar{\mu}_V = -0.8$. In Fig. 18 we perform the calculation along the line $\bar{\mu}_H + \bar{\mu}_V = -1$. According to Fig. 16c, we will go from I_0 to I_2 through a

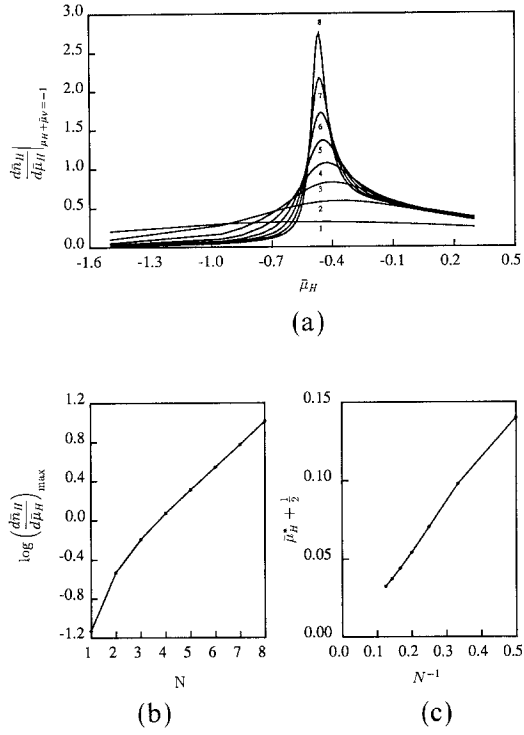

Fig. 17. (a) Derivative of H-rhombus density along the line $\bar{\mu}_H + \bar{\mu}_V = -1$ with $\delta = -0.8$. The sharp peaks indicate a phase transition. (b) Logarithm of the peak heights versus the system sizes. Linear behavior for large sizes reveals exponentially diverging peaks, which in turn suggests a first-order phase transition. (c) The peak positions shift toward $\bar{\mu}_H = -1/2$ obeying an inverse power law.

Table II. Peak Heights and Positions of the First Derivative of Density of H-rhombi with Respect to $\bar{\mu}_H$ along the Line $\bar{\mu}_H + \bar{\mu}_V = -1$ with $\delta = -0.8$[a]

	$N=3$	$N=4$	$N=5$	$N=6$	$N=7$	$N=8$
$d\bar{n}_H/d\bar{\mu}_H$	0.41229	0.53685	0.68233	0.86082	1.0869	1.38122
$\bar{\mu}_H^*$	−0.40220	−0.42970	−0.44581	−0.45594	−0.46275	−0.46757

[a] The peak heights fit well to the form $\exp(\sigma N)$ with $\sigma = 0.241 \pm 0.002$ (see Fig. 17b). The positions of the peaks shift toward $-1/2$ obeying an inverse power law: $\bar{\mu}_H^*(N) + 1/2 = (0.258 \pm 0.004)/N$ (see Fig. 17c).

first-order transition. Figure 17a shows the derivative of H-rhombus density. Sharp peaks indicate a phase transition. The peak heights for various finite-size systems, as well as their locations determined by Newton's method, are listed in Table II. For two-dimensional, infinitely long strips the susceptibilities for finite-width systems at a first-order transition usually diverge as $N^{\omega}\exp(\sigma N)$, where N is the width of the system and ω is a constant ($\omega = 2$ for the Ising model). Our results show (Fig. 17b) that $\omega = 0$ in this case, with $\sigma = 0.241 \pm 0.002$. The locations of the peaks converge very well toward $\bar{\mu}_H = \bar{\mu}_V = -1/2$, with an inverse power law, as is shown in Fig. 17c.

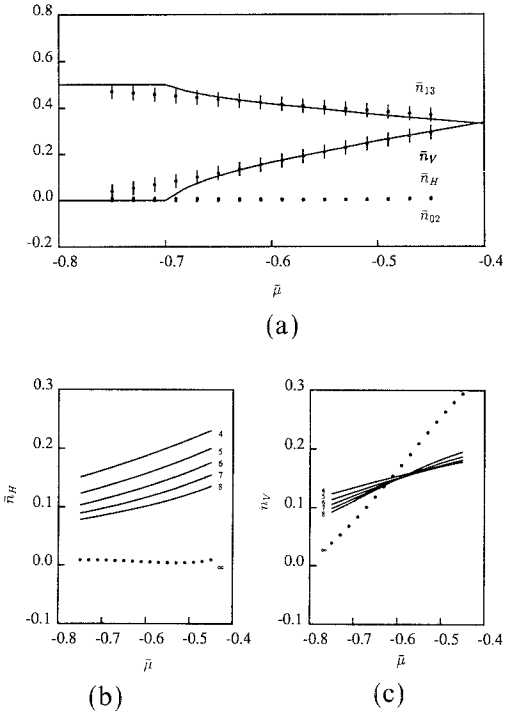

Fig. 18. (a) The solid curves are exact densities of V-rhombi and tilted squares of I_2 phase. The corresponding dots are the extrapolated densities of V-rhombi and tilted squares along the $I_0 \oplus I_2$ coexistence line with $\delta = -0.8$. Extrapolation errors are estimated and are rather subjective. The lowest dots are the extrapolated densities of (02)-type squares and H-rhombi; thus, there are essentially no such squares and rhombi. (b) The finite-size data of H-rhombus density along with the extrapolation results (the dots). The extrapolation is performed by fitting the data to the form $A + B/N$. Thus, H-rhombus density is essentially zero, indicating that the boundary condition picks up I_2 phase. (c) Densities of V-rhombi at finite sizes and their extrapolations (the dots). From (a) we see that extrapolated values agree with exact values tolerably well except close to the transition point, where the problem may simply be that we have underestimated our extrapolation errors.

It is interesting to note that our boundary condition breaks the symmetry between I_0 and I_2, so that on the phase coexistence line, only one phase will be observed. We argue that the boundary condition selects I_2, because near the C–IC transition I_0 and I_2 have different surface free energies. For I_2 the surface contribution is $\propto(-N^{-0.5})$, while for I_0 it is of the form $-N^{-1}$.[56] Thus we only see I_2 phase. Of course, in the thermodynamic limit the surface contribution vanishes and the symmetry between the two phases is restored. Figure 18 very convincingly shows such symmetry breaking due to boundary effects.

As we increase the value of $\bar{\delta}$ (thus also the value of δ), we see from Fig. 16 that the phase coexistence line should vanish and the quasicrystal

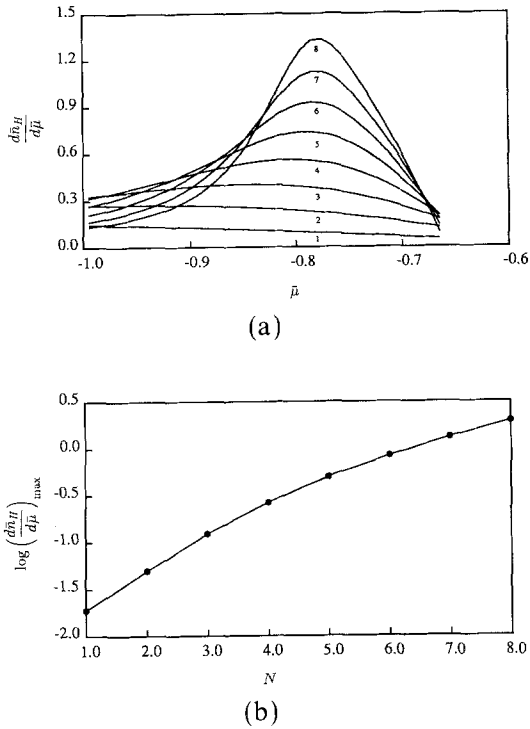

Fig. 19. (a) Derivatives of horizontal rhombus density for finite-size systems along the line $\bar{\mu}_H = \bar{\mu}_V \equiv \bar{\mu}$ with $\delta = 1.4$. Developing peaks suggest a phase transition from C_{13} to the quasicrystal phase. Notice that peak positions remain below $\bar{\mu} = -\log 2$, indicating $\pi^2 + 24b > 0$. (b) Logarithm of the peak heights versus the system sizes. The exponential nature of the peaks is not obvious, either due to weakness of the first-order transition, or else revealing a failure of Landau theory concerning the order of the transition. Much larger systems may be needed to be able to observe the expected exponentially diverging behavior.

phase touches the C_{13} phase. Numerically we find this happens at $\bar{\delta} = \delta = 0.55 \pm 0.05$, which Landau theory identifies as the parameter a. The error bar quoted here is rather subjective. When $\delta > a$, Landau theory predicts that along the line $\mu_H = \mu_V$ a first-order phase transition takes place at a point given by Eq. (108). Figure 19 shows the derivatives of H-rhombus density for finite-size systems along the line $\bar{\mu}_H = \bar{\mu}_V \equiv \bar{\mu}$ at a value $\bar{\delta} = 1.4$. Developing peaks suggest a phase transition. Although the expected exponential nature of the peak divergence is not apparent, due to the weakness of the phase transition, the fact that peaks stay away from $\bar{\mu} = -\log 2$ clearly suggests that such a transition is first order, because a continuous transition would yield a transition at $\bar{\mu} = -\log 2$. Note that our previous assumption that $\pi^2 + 24b > 0$ [after Eq. (106)] is confirmed by the fact that peaks converge toward a point below $\bar{\mu} = -\log 2$, according to Eq. (108).

From the above results we conclude that numerical data support the phase diagram proposed by Landau theory near the multicritical point A (and B, simply by symmetry). One important ingredient is the value of a, which we know comes from domain wall interactions. Unfortunately, we have been unable to derive its value analytically.

6. MISCELLANEOUS TOPICS AND CONCLUSIONS

In this section we shall discuss some of the features of the model that we did not cover or merely mentioned in the previously sections. Most of the questions that we still do not have clear answers to concern the nature of the quasicrystal phase. Description of the quasicrystal phase by means of domain walls provides a powerful way to explore the structure of the phase diagram. However, with regard to the detailed nature of the quasicrystal phase and related phase transitions our success has been so far very limited. Because of the rapid increase of the transfer matrix dimensionality, the largest system we could study has width 8, which makes finite-size scaling analysis extremely difficult. In this section we give numerical values of phason elastic constants and address the possibility of coexistence of phason strained quasicrystal states on the Δ_8 axis, the critical nature of the quasicrystal phase, and finite-size scaling behavior of the free energy density. We also point out the interesting connection between our tiling model and the one-dimensional Hubbard model, and compare the phase diagrams of these two models.

6.1. Phason Elastic Constants

In this subsection we present the values of phason elastic constants. Elser and Henley suggest that entropy density in random tiling models is in general maximum at the perfect quasicrystal state, with

$$\sigma = \sigma_0 - \tfrac{1}{2} \sum_{ijkl} K_{ijkl} E_{ij} E_{kl} \tag{109}$$

for small phason strains, where K_{ijkl} are phason elastic constants. The sum in Eq. (109) should transform as the unit representation of the group σ_{8v}. Note that the two indices of the phason strain matrix element E_{ij} transform as a two-dimensional vector in parallel and perpendicular spaces, respectively; thus, the group-theoretic analysis is exactly the same as that for the phason elastic free energy.[33] One finds three quadratic invariants associated with three independent phason elastic constants,

$$\begin{aligned} I_1 &= E_{xx}E_{xx} + E_{yy}E_{yy} + 2E_{xx}E_{yy} \\ I_2 &= E_{xy}E_{xy} + E_{yx}E_{yx} - 2E_{xy}E_{yx} \\ I_3 &= E_{xx}E_{xx} + E_{yy}E_{yy} - 2E_{xx}E_{yy} \\ &\quad + E_{xy}E_{xy} + E_{yx}E_{yx} + 2E_{xy}E_{yx} \end{aligned} \tag{110}$$

and Eq. (109) becomes

$$\sigma = \sigma_0 - \tfrac{1}{2}(K_1 I_1 + K_2 I_2 + K_3 I_3) \tag{111}$$

Note that in the 4-fold symmetric subspace $\Delta_x = \Delta_y = \Delta_2 = 0$ the phason strain matrix is diagonal, according to Eq. (28), $E_{xy} = E_{yx} = 0$ and $E_{xx} = E_{yy}$. In this case only I_1 is nonzero. Thus we have

$$\sigma = \sigma_0 - 2K_1 E_{xx}^2 \tag{112}$$

so that

$$K_1 = -\frac{1}{4} \frac{d^2\sigma}{dE_{xx}^2}\bigg|_{E_{xx} = E_{yy}} \tag{113}$$

Similarly, in the subspace $\Delta_x = \Delta_y = \Delta_4 = 0$ the phason strain matrix is also diagonal, $E_{xy} = E_{yx} = 0$ and $E_{xx} = -E_{yy}$, so that only I_3 is nonzero. We then have

$$\sigma = \sigma_0 - 2K_3 E_{xx}^2 \tag{114}$$

and

$$K_3 = -\frac{1}{4} \frac{d^2\sigma}{dE_{xx}^2}\bigg|_{E_{xx} = -E_{yy}} \tag{115}$$

Finally, by staying in the subspace $\Delta_x = -\Delta_y$, $\Delta_2 = 0$, and $\Delta_4 = 0$, we can maintain the relations $E_{xy} = -E_{yx}$ and $E_{xx} = E_{yy} = 0$ among the phason strain components, so that only I_2 has nonzero value. In this case

$$\sigma = \sigma_0 - 2K_2 E_{xy}^2 \tag{116}$$

and

$$K_2 = -\frac{1}{4}\frac{d^2\sigma}{dE_{xy}^2}\bigg|_{E_{xy} = -E_{yx}} \tag{117}$$

Table III lists the phason elastic constants K_1 and K_3 calculated from finite systems with sizes from 1 to 8. The extrapolated data $K_1 = 0.26 \pm 0.01$ and $K_3 = 0.342 \pm 0.008$ are obtained by fitting to the form $A + B/N$. We assume corrections of this form because our free boundary conditions generate a surface term inversely proportional to the system width N, in both free energy density and tile densities. More studies on finite-size corrections to the free energy can be found in Section 6.4. Finite-size analysis fails to give consistent results for K_2 due to slow convergence of the data. Instead we can only give an estimated range $0.35 < K_2 < 0.58$. Notice that the quadratic invariants in Eq. (110) are either perfect squares or sums of perfect squares of phason strain components; thus, stability conditions only require that the K's be positive. Our numerical results are consistent with these requirements.

6.2. Coexistence of Phason Strained Quasicrystal States on the Δ_8 Axis

The problem of whether quasicrystal states can coexist along the Δ_8 axis is closely related to the values of phason elastic constants. Just as we

Table III. Phason Elastic Constants Calculated from Systems with Different Sizes[a]

	$N=3$	$N=4$	$N=5$	$N=6$	$N=7$	$N=8$	$N=\infty$
$K_1^{(xx)}$	0.35020	0.32761	0.31525	0.30751	0.30241	0.29854	0.26 ± 0.01
$K_1^{(yy)}$	0.49715	0.42652	0.38782	0.36353	0.34732	0.33608	0.26 ± 0.01
$K_2^{(xy)}$	0.19078	0.19774	0.21029	0.22465	0.23918	0.25312	>0.35
$K_2^{(yx)}$	1.06121	1.08892	1.05866	1.00911	0.95785	0.91120	<0.58
$K_3^{(xx)}$	0.57705	0.50820	0.47146	0.44756	0.43128	0.41963	0.340 ± 0.008
$K_3^{(yy)}$	0.55757	0.49302	0.45977	0.43916	0.42495	0.41480	0.344 ± 0.007

[a] Both K_1 and K_3 are obtained near the point $\Delta_8 = 0.0308$ on the 8-fold symmetric line. For finite systems E_{xx} and E_{yy} have different values, which yields two sequences for K_1 and K_3 using E_{xx} and E_{yy} respectively. Similarly, E_{xy} and E_{yx} yield two sequences for K_2. In the thermodynamic limit these two sequences yield consistent values for K_1 and for K_3. For K_2 we deduce only bounds.

did in Section 4.1 when discussing Fig. 10, consider the canonical ensemble in which the value d_8 takes an arbitrary but fixed value. According to Eq. (111) we have the Helmholtz free energy density for small phason strains,

$$f(d_8) = -\sigma_0 + \tfrac{1}{2}(K_1 I_1 + K_2 I_2 + K_3 I_3) \tag{118}$$

From Eqs. (28) and (110) we have

$$d_8 = \tfrac{1}{2} \det \mathsf{E} \tag{119}$$

and

$$I_1 + I_2 - I_3 = 4 \det \mathsf{E} \tag{120}$$

Thus, Eq. (118) can be rewritten as

$$f(d_8) = -\sigma_0 + 4K_1 d_8 + \tfrac{1}{2}(K_2 - K_1) I_2 + \tfrac{1}{2}(K_3 + K_1) I_3 \tag{121}$$

Since $K_2 - K_1$, I_2, and I_3 are all nonnegative, if $d_8 > 0$, the most stable states correspond to those with $I_2 = I_3 = 0$. Note that $d_8 = \frac{1}{2}E_{xx}^2$ is always positive in this case. In this case Eq. (121) becomes a straight line with slope $4K_1$. Comparing the slope $2\sigma_0$ of the dashed line passing through $d_8 = 1/2$ in Fig. 10a, we see that the condition

$$K_1 \leqslant \tfrac{1}{2}\sigma_0 \tag{122}$$

guarantees the coexistence of phason strained quasicrystal states. However, the value of $K_1 = 0.26 \pm 0.01$ obtained in Section 6.1 is very close to $\frac{1}{2}\sigma_0 = 0.2620 \pm 0.0003$, so we cannot make any conclusions. Numerical study of rhombus densities in the region between C_1 and C_2 in Fig. 9b also fails to offer any insight, which is probably due to the closeness of K_1 and $\frac{1}{2}\sigma_0$.

When $d_8 < 0$, from Eqs. (119) and (120) we see that the most stable states correspond to those with $I_1 = I_2 = 0$, and Eq. (121) reduces to

$$f(d_8) = -\sigma_0 - 4K_3 d_8 \tag{123}$$

Note that $d_8 = -\frac{1}{2}E_{xx}^2$ is always negative in this case. Also note that the line in Eq. (123) lies in between the two broken lines in Fig. 10a because $2K_3 > \sigma_0$; we thus conclude that phason strained quasicrystal states cannot be stable when $d_8 < 0$, which is why ϕ directly enters the coexisting incommensurate phase.

Finally, assume the condition in (122) is satisfied; then point C_1 in Fig. 9b corresponds to a critical point. $C_1 C_2$ is a first-order line across

which a first-order transition takes place between two phases related by a symmetry operation—a 45° rotation. This phase transition becomes continuous as we approach point C_1.

6.3. Quasicrystal as a Critical Phase

From the point of view that 2D quasicrystals have quasi-long-range translational order generating power-law diffraction peaks, we know that in general 2D quasicrystal phases correspond to certain kinds of critical phases. The question of whether the random tiling model gives a critical phase has been explored by several authors.[21,22] In Monte Carlo simulations a height–height correlation function in perpendicular space is calculated and is found to diverge as log N, where N is the system size. This directly shows the existence of quasi-long-range translational order.

In the transfer matrix approach this quasi-long-range translational order shows up in the asymptotic degeneracy of the two largest eigenvalues as system size increases. Table IV lists the two largest eigenvalues at $\bar{\mu}_H = \bar{\mu}_V = -0.127$ and $\bar{\mu}_{02} = -0.254$, which corresponds to a point $\Delta_8 = 0.0308$ on the 8-fold symmetric line. The tendency of the magnitude of the ratio between the two largest eigenvalues to go toward one is apparent. We have applied the θ-algorithm[57] as well as fitted to the form $\exp(s/N)$, both yielding consistent extrapolated ratios which are close to one. It is conceivable that s is related to a critical exponent $x = s/\pi\zeta$, where ζ is an "anisotropy factor." It is important to realize that the 8-fold symmetric state is not unique in being critical. The entire quasicrystal phase and I phases are critical.

6.4. Finite-Size Scaling of Free Energy Density

The finite-size scaling behavior of free energy density for incommensurate systems has received considerable interest recently.[39,43,58] Both

Table IV. The Largest and Second Largest Eigenvalues of the Transfer Matrix at the Point $\Delta_8 = 0.0308$ on the 8-fold Symmetric Line[a]

	$N=3$	$N=4$	$N=5$	$N=6$	$N=7$	$N=8$
λ_0	6.40725	8.13410	10.3654	13.2420	16.9464	21.7137
λ_1	2.97463	4.52674	6.41056	8.80387	11.8875	15.8718
λ_0/λ_1	2.15396	1.79690	1.61692	1.50411	1.42556	1.36807

[a] The ratios of these two eigenvalues approach 1 in the thermodynamic limit, as one can see from the table. The θ-algorithm gives the extrapolated ratio 1.0 ± 0.1, while fitting to the form $\exp(s/N)$ yields a result $s = 2.684 \pm 0.007$.

analytical and numerical results reveal the applicability of conformal theory. However, previous studies have all concentrated on systems which are incommensurate in one direction but commensurate in the other direction; thus, for the general quasicrystal phase the applicability of conformal theory remains to be tested. Of particular interest is the question of how the universal amplitude of the quasicrystal free energy is related to the amplitudes of the I_0 and I_2 phases.

Inspired by the previous successes, we assume that the finite-size scaling behavior of the quasicrystal free energy has the following form:

$$F = F_\infty + \frac{F_s}{N} - \frac{\pi}{24N^2} A \tag{124}$$

In Table V we list the results of fitting the numerical data to Eq. (124) at the point $\Delta_8 = 0.0308$ on the 8-fold symmetric line, along with the extrapolation results using the θ-algorithm. The relatively stable coefficients, and the rapid convergence of the first term toward the value from the θ-algorithm, all suggest that Eq. (124) is plausible.

In order to check the agreement with conformal theory, one has to show that the amplitude A is really the product of the conformal charge with the anisotropy factor. Since the anisotropy factor is in general difficult to calculate, this approach may be impractical. In principle, examination of the transfer matrix eigenvalue spectrum will yield conformal charge and anisotropy factors separately. But Woynarovich[59] has recently pointed out that models consisting of two interacting $c = 1$ fermion fields are in general not conformally invariant. Conformal invariance is restored only at certain special points where the two Fermi velocities coincide, resulting in

Table V. Finite-Size Scaling Analysis of the Free Energy Density Inside the Quasicrystal Phase[a]

	$N=3$	$N=4$	$N=5$	$N=6$	$N=7$	$N=8$
F_N	−0.61914	−0.52402	−0.46769	−0.43057	−0.40429	−0.38474
F_∞	−0.23740	−0.24441	−0.24807	−0.24996	−0.25100	−0.25158
F_s	−1.13615	−1.10109	−1.07551	−1.05849	−1.04701	−1.03952
A	0.20812	0.52957	0.86455	1.15343	1.39264	1.57765

[a] The free energy is calculated at the same point as in Table IV. We use three data points F_{N-2}, F_{N-1}, F_N to fit to the form of Eq. (124). The corresponding coefficients F_∞, F_s, and A are listed under the column with size N. The relatively stable trends of these coefficients support Eq. (124). The extrapolated value of the free energy from the θ-algorithm is -0.2530 ± 0.0008.

a model with $c=2$. Thus, even if our model is in general conformally noninvariant, it is still interesting to ask whether the perfect quasicrystal point in our model corresponds to such a special point with $c=2$.

6.5. Transitions from the Incommensurate to the Quasicrystal Phase

In this subsection we discuss the nature of phase transitions from the incommensurate phases to the quasicrystal phase. We start with the Landau theory equations (103) and (104) and consider three cases separately according to the value of $\delta - a$.

First consider the case $\delta - a > 0$, which corresponds to Fig. 16a. Assuming, temporarily, that the transition between I_0 and Q is continuous, then along the phase boundary between I_0 and Q, $d_V = 0$ and d_H takes on the values in I_0. We see that Eq. (103) can be satisfied, but Eq. (104) becomes

$$-\tilde{\mu}_V - \tfrac{1}{2}(\delta - a)\, d_H + b d_H^2 = 0 \tag{125}$$

which is not consistent with Fig. 16a, since at $\tilde{\mu}_H = 0$, $d_H = 0$ (continuous transition from I_0 to C_{13}) and thus $\tilde{\mu}_V = 0$. We thus conclude that the phase transition must be first order.

Next consider $\delta - a = 0$. In this case Eqs. (103) and (104) are consistent with having a continuous phase transition between I_0 and Q. Furthermore, we can derive the linear behavior of the phase boundary

$$\tilde{\mu}_V = \frac{8b}{\pi^2}\, \tilde{\mu}_H \tag{126}$$

Finally, in the case $\delta - a < 0$, we shall show that the transition is continuous. For continuous transitions the phase boundary between Q and I_0 can be obtained from Eqs. (103) and (104) by letting $d_V = 0$,

$$\tilde{\mu}_H = \frac{\pi^2}{8}\, d_H^2 \tag{127}$$

$$\tilde{\mu}_V = -\frac{1}{2}(\delta - a)\, d_H + b d_H^2$$

In order to check that this continuous transition is not preempted by first-order transitions, let us compare the free energy densities of I_0 and Q. From Eq. (74) we have

$$\frac{\partial f_Q}{\partial \tilde{\mu}_H} = -d_H + \frac{1}{2} d_H d_V \tag{128}$$

$$\frac{\partial f_Q}{\partial \tilde{\mu}_V} = -d_V + \frac{1}{2} d_H d_V \tag{129}$$

where we have used Eqs. (103) and (104). Since $f_Q = f_{I_0}$ when $d_V = 0$, and f_{I_0} is independent of $\tilde{\mu}_V$, Eq. (129) indicates that $f_Q < f_{I_0}$ when $d_V > 0$. Therefore the quasicrystal phase Q is more stable than I_0 for $\tilde{\mu}_V$ greater than the critical value given by Eq. (127). Thus, the transition between Q and I_0 is continuous for $\delta - a < 0$.

Numerical verification of the picture described above has not been totally successful. Derivatives of tile densities have bumps as one crosses the phase boundary between I_0 (or I_2) and Q at finite sizes. Power law peaks correspond to continuous transitions, while exponential peaks suggest first-order transitions. For $\delta < a$ numerical data show power law peaks that are consistent with continuous transitions predicted by Landau theory, because peak heights form an almost straight line on a log-log plot (Fig. 20). But Landau theory predicts $\bar{n}_{02}$ is linear at the phase boundary, so the line should have zero slope. Clearly, the numerical data do not support Landau theory in this respect. Also, in the case $\delta > a$ the numerical data[34] fail to show an exponential dependence on N, just as in the case of $C_{13} \leftrightarrow Q$ (Fig. 19).

6.6. Connection with the Hubbard Model

The one-dimensional Hubbard[60] model is defined by the Hamiltonian

$$H = -\sum_{i=1}^{N} \sum_{\sigma} (c_{i+1,\sigma}^{\dagger} c_{i,\sigma} + c_{i,\sigma}^{\dagger} c_{i+1,\sigma}) + 4U \sum_{i=1}^{N} n_{i\uparrow} n_{i\downarrow} - \mu r - mh \tag{130}$$

where $c_{i,\sigma}$ ($\sigma = \pm 1$) are the fermion operators for the electrons, $n_{i,\sigma} = c_{i,\sigma}^{\dagger} c_{i,\sigma}$ is the electron number operator at the ith site with spin σ, and μ and h are the chemical potential and magnetic field. $r = \sum_{i=1}^{N} (n_{i\uparrow} + n_{i\downarrow})$ is the total electron density and $m = \sum_{i=1}^{N} (n_{i\uparrow} - n_{i\downarrow})$ is the magnetization. We have absorbed a factor of 1/2 times the electron magnetic moment into the definition of h.

Our tiling model resembles the one-dimensional Hubbard model in some respects. Electrons with up and down spins correspond to two types of domain walls in our tiling model. Just like two domain walls within the same family, two electrons of the same spin never occupy the same site. Incommensurate phases with only one type of domain wall correspond to

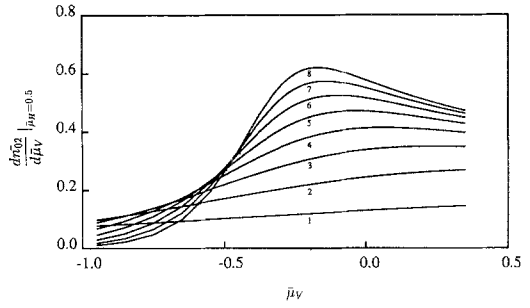

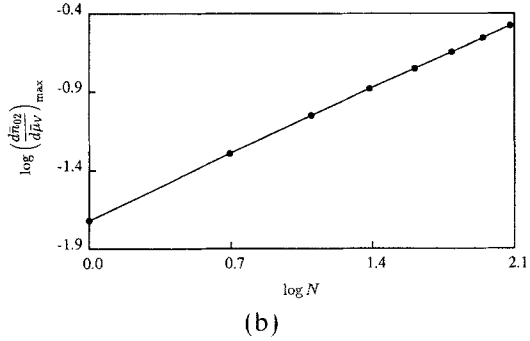

Fig. 20. (a) $d\bar{n}_{02}/d\bar{\mu}_V$ along the line $\bar{\mu}_H = 0.5$ for finite sizes with $\delta = 0$. Developing peaks indicate a transition from I_0 to the quasicrystal phase Q. (b) A log–log plot of peak heights in (a) versus system sizes. The almost linear behavior suggests a continuous transition, consistent with the prediction of Landau theory.

phases of the Hubbard model with only one electron spin. Our phason strained quasicrystal phase Q corresponds to the most general phase in the Hubbard model, in which both electron densities take general values. Since many details of our conjectured tiling model phase diagrams rest on the assumed (but unproven) applicability of Landau expansions, it is worth noting the validity of such expansions in the case of the exactly solvable 1D Hubbard model.

Using the Bethe ansatz solution by Lieb and Wu,[61] Takahashi[62] studied the ground-state phase diagram for both repulsive ($U > 0$) and attractive ($U < 0$) electron interactions. The phase diagrams shown in Fig. 21, particularly in the vicinity of the point marked A in Fig. 21b, should be compared with the phase diagrams Figs. 16a–16c of our tiling

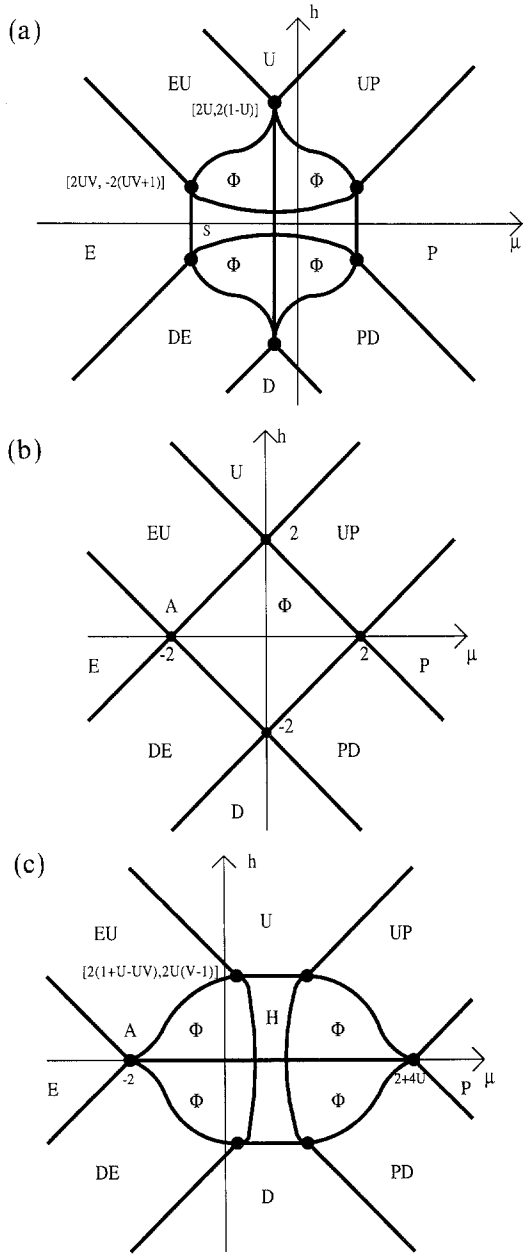

Fig. 21. Ground-state phase diagram of the one-dimensional Hubbard model. All transitions are continuous. (a) $U<0$. Here S is the "superconducting" phase, in which magnetization $m=0$. (b) $U=0$. (c) $U>0$. Here H is the half-filled phase. $V=(1+1/U^2)^{1/2}$. Point A in (b) and (c) should be compared with point A in Fig. 16b.

model. Let ξ and η be up- and down-spin electron densities, respectively. Different phase regions are defined as follows. Four ordered phases are

Phase E: $\xi = \eta = 0$
Phase U: $\xi = 1$ and $\eta = 0$
Phase P: $\xi = \eta = 1$
Phase D: $\xi = 0$ and $\eta = 1$

Four incommensurate phases are

Phase EU: $0 < \xi < 1$ and $\eta = 0$
Phase UP: $\xi = 1$ and $0 < \eta < 1$
Phase PD: $0 < \xi < 1$ and $\eta = 1$
Phase DE: $\xi = 0$ and $0 < \eta < 1$

Φ is the most general phase corresponding to our quasicrystalline phase Q. For those phases which touch point A in Fig. 21, we can identify phases E, EU, DE, and Φ with C_{13}, I_2, I_0, and Q in the tiling model, respectively. S is the superconducting phase, in which $\xi = \eta$, and H is the half-filled phase, in which $\xi + \eta = 1$. Phases S and H have no tiling model analogies.

Phase EU transforms into phases E and U through C–IC transitions. Similarly for UP, PD, and DE. The phase boundaries corresponding to these C–IC transitions can be worked out exactly, since the model reduces to the free fermion model:

$$\begin{aligned} &\text{E–EU–U:} \quad h + \mu = \pm 2 \\ &\text{U–UP–P:} \quad h - \mu = -4U \pm 2 \\ &\text{P–PD–D:} \quad h + \mu = 4U \pm 2 \\ &\text{D–DE–E:} \quad h - \mu = \pm 2 \end{aligned} \tag{131}$$

However, the transition between E and Φ in the Hubbard model is always continuous regardless of the sign of U, in contrast to the tiling model, in which the transition between C_{13} and Q is first order for $\delta > 0$, and passes through an intermediate incommensurate phase $I_0 \oplus I_2$ when $\delta < 0$. One of the unanswered questions in our tiling model is the nature of phase transitions between I_α and Q. The corresponding phase transition between EU and Φ in the Hubbard model is always continuous. Furthermore, in the direction $h + \mu = \text{const}$ the transition shows the nature of a C–IC transition.

Landau expansion of the ground state energy can be obtained exactly from Lieb and Wu's integral equations.[63,64] We find

$$E(\xi, \eta) = E_0(\xi) + E_0(\eta) + I(\xi, \eta) - (\xi + \eta)\mu - (\xi - \eta)h \tag{132}$$

where, for small x,

$$E_0(x) = -2x + \frac{\pi^2}{3}x^3 + \cdots \tag{133}$$

and, for $U > 0$,

$$I(\xi, \eta) = \pi^2 \xi\eta(\xi + \eta) + \cdots \tag{134}$$

Note that the leading order of the interaction $I(\xi, \eta)$ is cubic in electron densities rather than quadratic. This form should be compared with the Landau expansion of the tiling model, Eq. (71) in Section 3.4. That the transitions among the phases E, EU, DE, and Φ in the Hubbard model are continuous is certainly due to the absence of the quadratic term in Eq. (134). Also, it should be pointed out that $I(\xi, \eta)$ is not an analytic function of its two arguments, because the next-order term is of the form $\max(\xi^2, \eta^2)\,\xi\eta$. This nonanalyticity creates a third-order phase transition as h passes through 0. Such a breakdown of the Landau expansion could also exist in our tiling model, but will not change any major features of the phase diagram except for the additional third-order phase transition. For $U < 0$, $I(\xi, \eta) \propto \min(\xi, \eta)$ to the leading order, indicating that electrons of different spins tend to stick to each other, thereby increasing the effective chemical potentials of these electron pairs, rather than scattering off of each other as in the repulsive $U > 0$ case. Again the $\xi\eta$ term does not appear.

We close this subsection by pointing out that substantial differences between our tiling model and the one-dimensional Hubbard model do exist. First of all, in the tiling model different families of domain wall in general run in different directions, while up and down fermions in the Hubbard model all go in the same (time) direction. Also, in the tiling model, the density of domain wall crossing is completely determined by the densities of domain walls themselves, a fact which is reflected in the quadratic constraint (30). But for the Hubbard model, the density of electron pairs is only statistically determined, which is reflected by the absence of the quadratic term $\xi\eta$ in Eq. (134). Thus, although these two models are rather similar, they are certainly not completely equivalent. Our principal conclusion from this study of the Hubbard model is that Landau expansions of the sort in Section 3.4 may accurately represent the free energy for small domain wall densities.

6.7. Generalizations to Other Models

In two dimensions, models with 10- and 12-fold rotational symmetries have been studied quite extensively in the past several years. The 10-fold model has two types of Penrose rhombi—the thin rhombus with 36° angles and the fat rhombus with 72° angles. Bonds are oriented in one of five directions, so we can construct a total of five different types of de Bruijn lines by connecting centers of parallel edges. As in our present model, domain walls of the same type do not touch each other and there is an effective repulsion among them. C–IC transitions take place between rhombic crystal phases and certain incommensurate phases similar to I_α in our model.

The 12-fold model can be described in terms of triangles and squares of equal edge length. This model was first studied by Kawamura[37] as a model of two-dimensional liquid. Here the notion of de Bruijn lines is lost, since the triangles lack parallel edges. However, in describing the transition between the triangular or square lattices and the mixed phase, one finds that domain walls can be identified which form a hexagonal network. These domain walls are more highly constrained than those in our present model. Fluctuations of a single wall are forbidden, but creation and annihilation of walls are permitted. Thus, in the 12-fold model one faces a completely new situation and description in terms of striped incommensurate phases is no longer appropriate. Kawamura found a first-order transition between the triangular phase and the amorphous (quasicrystal) phase, similar to our phase diagram in Fig. 9a along the Δ_8 axis where the strain-free quasicrystal phase and the square phases are separated by a first-order transition.

In three dimensions quasicrystal phases may be random packings of rhombohedra. Instead of de Bruijn lines, we then have de Bruijn planes. As in two dimensions, de Bruijn planes of the same type do not touch each other and we then have an effective repulsion among them, a situation similar to the steric interaction of fluid membranes studied by Helfrich[65] and Lipowsky *et al.*,[66,67] where out-of-plane fluctuations are responsible for the membrane entropy as well as membrane repulsion. Unlike 2-dimensional random walkers, where fluctuations grow like $\sqrt{N}$ for N steps, fluctuations of a de Bruijn plane are proportional to $\log L$, where L is the size of the plane. The logarithm follows because tilting of a plane induces a phason strain. Hence the free energy of a de Bruijn plane should go as $|\nabla u|^2$, where u is the out-of-plane fluctuation.

Thus, when two de Bruijn planes are at a distance l apart, they will touch each other once in an area proportional to $\exp(\alpha l)$. The interaction between the two membranes, expected to be proportional to the density of

contacts, is proportional to $d\exp(-\alpha/d)$, where $d=1/l$ the de Bruijn plane density. So the free energy density of such a system in the small-density limit is

$$f=-d(\mu+s_0)+s_1 d\exp(-\alpha/d)+\cdots \tag{135}$$

where μ and s_0 are the chemical potential and entropy of the planes. Minimizing the free energy yields a weak logarithmic singularity in d,

$$d\simeq -\frac{1}{\log(\mu+s_0)} \tag{136}$$

This result differs from that of Helfrich because there is no gradient energy associated with Helfrich's membranes.

6.8. CONCLUSIONS

In summary, we have studied a two-dimensional random tiling model of a quasicrystal. From the point of view that the quasicrystal phase can be described by two sets of domain walls interacting with each other, we constructed a Landau theory which successfully describes most of the qualitative features of the phase diagram near the multicritical points. Numerical study by the transfer matrix approach confirms most of the conclusions of Landau theory. We found a critical quasicrystal phase surrounded by many other phases, whose exact solutions exist. From crystal phases, the system can either enter the quasicrystal phase directly through a first-order phase transition, which at some special parameter combinations can become continuous, or go through an intermediate incommensurate phase by two successive phase transitions corresponding to the introduction of incommensurability in two different directions. While the first transition is identified as the usual C–IC phase transition, the Landau theory suggests that the second one can be either first order or continuous.

The free energy density of the quasicrystal phase has the usual finite-size scaling behavior predicted by the conformal theory, but more careful study is needed for quantitative comparison. We explain why the strain-free states should occupy a finite region. That is, we observe locking of the concentration on irrational value resulting from the nonlinear constraint. The entropy density for these states and phason elastic constant are calculated, and our numerical results support Elser and Henley's conjecture that states with the highest rotational symmetry have maximum entropy.

There are still some questions left unanswered. The critical behavior of the multicritical points A and B is not clear. The physical origin of the constant a, defined in Eq. (74) representing the entropy reduction associated with crossings of perpendicular domain wall families, whose value is found

to be 0.55 ± 0.05 in Section 5.3, needs to be further explored. About the nature of the transition between the incommensurate I phase and the quasicrystal phase, although Landau theory makes some predictions, numerical evidence is rather weak and unsatisfactory. Also, whether coexisting phason strained quasicrystal states appear on the Δ_8 axis is still unanswered. Finally, the statistical mechanical nature of the quasicrystal phase is basically unexplored. Obviously, an exact solution of our model will give definite answers to all these questions. However, the existence of such an exact solution itself is a very attractive and challenging problem. Our initial examination of the problem suggests the Bethe Ansatz fails inside the quasicrystal phase.

ACKNOWLEDGMENTS

We wish to thank Prof. Griffiths for many useful discussions, especially for his transformation of chemical potentials between the lattice model and the original tiling model. We also acknowledge useful discussions with Dr. S. Burkov, Prof. C. L. Henley, Prof. J. F. Nagle, and Prof. D. R. Nelson. This work is supported in part by the National Science Foundation, grant DMR-8918810, and by the Donors Petroleum Research Fund. M. W. acknowledges support of the A. P. Sloan Foundation. Most of the numerical computation was done at the Pittsburgh Supercomputer Center and their service is gratefully acknowledged.

REFERENCES

1. D. Shechtman, I. Blech, D. Gratias, and J. W. Cahn, *Phys. Rev. Lett.* **53**:1951 (1984); for reviews see C. L. Henley, *Comm. Cond. Matter Phys.* **13**:58 (1987), and M. V. Jaric, ed., *Introduction to Quasicrystals* (Academic Press, 1988).
2. N. Wang, H. Chen, and K. H. Kuo, *Phys. Rev. Lett.* **59**:1010 (1987).
3. L. Bendersky, *Phys. Rev. Lett.* **55**:1461 (1985).
4. T. Ishimasa, H. V. Nissen, and Y. Fakano, *Phys. Rev. Lett.* **55**:51 (1985).
5. F. C. Frank, *Proc. R. Soc. Lond. A* **215**:43 (1952).
6. P. J. Steinhardt, D. R. Nelson, and M. Ronchetti, *Phys. Rev. Lett.* **47**:1297 (1981).
7. A. D. J. Haymet, *Phys. Rev. B* **27**:1275 (1983).
8. D. Shechtman and I. Blech, *Metall. Trans.* **16A**:1005 (1985).
9. P. Stephens and A. Goldman, *Phys. Rev. Lett.* **56**:1168 (1986).
10. N. G. de Bruijn, *Proc. K. Akad. Wet. A* **84**:39, 53 (1981).
11. D. Levine and P. Steinhardt, *Phys. Rev. B* **34**:596 (1986).
12. J. Socolar and P. Steinhardt, *Phys. Rev. B* **34**:617 (1986).
13. K. J. Strandburg and P. R. Dressel, *Phys. Rev. B* **41**:6071 (1990).
14. P. A. Kalugin, *JETP Lett.* **57**:467 (1989).
15. L. H. Tang and M. V. Jaric, *Phys. Rev. B* **41**:4524 (1990).
16. V. Elser, *Phys. Rev. Lett.* **54**:1730 (1985).
17. C. L. Henley, *J. Phys. A* **21**:1649 (1988).

18. M. Widom, K. J. Strandburg, and R. H. Swendsen, *Phys. Rev. Lett.* **57**:706 (1987).
19. P. W. Leung, C. L. Henley, and G. V. Chester, *Phys. Rev. B* **39**:446 (1989).
20. F. Lançon and L. Billard, *J. Phys.* (Paris) **49**:249 (1988).
21. K. J. Strandburg, L. H. Tang, and M. V. Jaric, *Phys. Rev. Lett.* **63**:314 (1989).
22. M. Widom, D. P. Deng, and C. L. Henley, *Phys. Rev. Lett.* **63**:310 (1989).
23. P. A. Bancel, P. A. Heiney, P. W. Stephens, A. I. Goldman, and P. M. Horn, *Phys. Rev. Lett.* **54**:2422 (1985).
24. A. P. Tsai, A. Inoue, and T. Masumoto, *Jpn. J. Appl. Phys. 2* **26**:L1505 (1987).
25. A. P. Tsai, A. Inoue, and T. Masumoto, *Jpn. J. Appl. Phys. 2* **27**:L1587 (1987).
26. C. A. Guryan, A. I. Goldman, P. W. Stephens, K. Hirga, A. P. Tsai, A. Inoue, and T. Masumoto, *Phys. Rev. Lett.* **62**:2409 (1989).
27. P. A. Bancel, *Phys. Rev. Lett.* **63**:2741 (1989).
28. M. Widom, in *Proceedings of the Adriatic Research Conference on Quasicrystals*, M. V. Jaric and S. Lundqvist, eds. (World Scientific, 1990).
29. C. Henley, in *Quasicrystal and Incommensurate Structures in Condensed Matter* (World Scientific, 1989).
30. Y. Ishii, *Phys. Rev. B* **39**:11862 (1989).
31. M. Audier and P. Guyot, in *Quasicrystals*, M. V. Jaric and S. Lundqvist, eds. (World Scientific, 1990), p. 74.
32. K. Hiraga, W. Sun, and F. J. Lincoln, *Jpn. J. Appl. Phys.* (1990), submitted.
33. J. E. S. Socolar, *Phys. Rev. B* **39**:10519 (1989).
34. W. Li, Ph.D. thesis, Department of Physics, Carnegie Mellon University, Pittsburgh, Pennsylvania (July 1991).
35. V. Elser, *Phys. Rev. B* **32**:4892 (1985).
36. L. J. Shaw and C. L. Henley, *J. Phys. A* (1990), submitted.
37. H. Kawamura, *Prog. Theor. Phys.* **70**:352 (1983).
38. E. H. Lieb and F. Y. Wu, in *Phase Transitions and Critical Phenomena*, Vol. 1, C. Domb and M. S. Green, eds. (Academic, London, 1972).
39. W. Li, H. Park, and M. Widom, *J. Phys. A* **23**:L573 (1990).
40. M. den Nijs, in *Phase Transitions and Critical Phenomena*, Vol. 12, C. Domb and J. L. Lebowitz, eds. (Academic, London, 1988).
41. V. L. Pokrovsky and A. L. Talapov, *Phys. Rev. Lett.* **42**:65 (1979).
42. H. W. J. Blöte and H. J. Hilhorst, *J. Phys. A* **15**:L631 (1982).
43. H. Park and M. Widom, *Phys. Rev. Lett.* **64**:1076 (1990).
44. D. P. Deng, Ph.D. thesis, Department of Physics, Carnegie Mellon University, Pittsburgh, Pennsylvania.
45. W. P. Orrick, Senior Thesis, Department of Physics, Princeton University, Princeton, New Jersey (1987).
46. P. Bancel, talk given at APS 1991 March meeting.
47. S. E. Burkov, Modeling decagonal quasicrystals: Random assembly of interpenetrating decagonal clusters, preprint (1990).
48. M. Fisher, Phases and phase diagrams: Gibbs' legacy today, in *Proceedings of the Gibbs Symposium*, Yale University, New Haven, Connecticut (1989), and references therein.
49. D. Yoshioka, B. I. Halperin, and P. A. Lee, *Phys. Lett.* **50**:1219 (1983).
50. R. B. Laughlin, *Phys. Rev. Lett.* **50**:1395 (1983).
51. D. A. Rabson, D. Mermin, D. S. Rokhsar, and D. C. Wright, *Rev. Mod. Phys.* **63**:699 (1991).
52. M. E. Fisher and D. R. Nelson, *Phys. Rev. Lett.* **32**:1350 (1974).
53. D. R. Nelson, J. M. Kosterlitz, and M. E. Fisher, *Phys. Rev. Lett.* **33**:813 (1974).
54. K. S. Liu and M. E. Fisher, *J. Low Temp. Phys.* **10**:655 (1973).

55. I. D. Lawrie and S. Sarbach, in *Phase Transitions and Critical Phenomena*, Vol. 9, C. Domb and J. L. Lebowitz, eds. (Academic, London, 1984).
56. W. Li and H. Park, *J. Phys. A* **24**:257 (1991).
57. M. N. Barber, I. Peschel, and P. A. Pearce, *J. Stat. Phys.* **37**:394 (1984).
58. H. Park and M. Widom, *J. Stat. Phys.* **61**:51 (1990).
59. F. Woynarovich, *J. Phys. A* **22**:4243 (1989).
60. J. Hubbard, *Proc. R. Soc. Lond. A* **276**:238 (1963); **277**:237 (1964).
61. E. H. Lieb and F. Y. Wu, *Phys. Rev. Lett.* **20**:1445 (1968).
62. M. Takahashi, *Prog. Theor. Phys.* **52**:103 (1974).
63. M. Suzuki, *Prog. Theor. Phys.* **42**:1076 (1969).
64. M. Takahashi, *Prog. Theor. Phys.* **44**:348 (1969).
65. W. Helfrich, *Z. Naturforsch.* **33a**:305 (1978).
66. R. Lipowsky and S. Leibler, *Phys. Rev. Lett.* **56**:2541 (1986).
67. R. Lipowsky and B. Zielinska, *Phys. Rev. Lett.* **62**:1572 (1989).